J. Fluid Mech. (2021), *vol*. 906, A2. © The Author(s), 2020.
Published by Cambridge University Press
doi:10.1017/jfm.2020.784

Reynolds number scaling of burning rates in spherical turbulent premixed flames

Tejas Kulkarni[1],†, **Romain Buttay**[2], **M. Houssem Kasbaoui**[3], **Antonio Attili**[4] **and Fabrizio Bisetti**[1]

[1]Department of Aerospace Engineering and Engineering Mechanics, University of Texas at Austin, Austin, TX 78712, USA

[2]Clean Combustion Research Center (CCRC), King Abdullah University of Science and Technology (KAUST), Thuwal 23955, Saudi Arabia

[3]Department of Aerospace and Mechanical Engineering, Arizona State University, Tempe, AZ 85281, USA

[4]School of Engineering, University of Edinburgh, Edinburgh EH9 3FD, UK

(Received 9 October 2019; revised 20 July 2020; accepted 8 September 2020)

In the flamelet regime of turbulent premixed combustion the enhancement in the burning rates originates primarily from surface wrinkling. In this work we investigate the Reynolds number dependence of burning rates of spherical turbulent premixed methane/air flames in decaying isotropic turbulence with direct numerical simulations. Several simulations are performed by varying the Reynolds number, while keeping the Karlovitz number the same, and the temporal evolution of the flame surface is compared across cases by combining the probability density function of the radial distance of the flame surface from the origin with the surface density function formalism. Because the mean area of the wrinkled flame surface normalized by the area of a sphere with radius equal to the mean flame radius is proportional to the product of the turbulent flame brush thickness and peak surface density within the brush, the temporal evolution of the brush and peak surface density are investigated separately. The brush thickness is shown to scale with the integral scale of the flow, evolving due to decaying velocity fluctuations and stretch. When normalized by the integral scale, the wrinkling scale defined as the inverse of the peak surface density is shown to scale with Reynolds number across simulations and as turbulence decays. As a result, the area ratio and the burning rate are found to increase as $Re_\lambda^{1.13}$, in agreement with recent experiments on spherical turbulent premixed flames. We observe that the area ratio does not vary with turbulent intensity when holding the Reynolds number constant.

Key words: turbulent reacting flows, isotropic turbulence

1. Introduction

Technical combustion devices operate in the turbulent regime in order to increase burning rates and achieve higher power densities than are otherwise possible in laminar flows. Turbulence modulates the reactive front surface area through wrinkling and the

† Email address for correspondence: tukulkarni@utexas.edu

mean burning rate per unit area through modifications to the flame structure. The former effect dominates over the latter in the wrinkled and thin reaction zone regimes (Borghi 1985; Peters 1988, 1999) and is the focus of the present study.

The dimensionless turbulent burning velocity S_T/S_L depends on a variety of dimensionless parameters such as the ratios of length and velocity scales of flame and turbulence, Reynolds, Karlovitz and Damköhler numbers. Here, S_T is the mean volumetric burning rate normalized by a density and a suitable reference area, while S_L is the propagation speed for a freely propagating laminar flame. Understanding the dependence of the turbulent burning velocity on various dimensionless groups is vital to turbulent premixed combustion modelling.

Early experiments on turbulent burning rates focused primarily on their dependence on the ratios u'/S_L and l/δ_L. Here u' is the turbulent velocity fluctuation, l the integral length scale of turbulence and δ_L the laminar flame thickness. Damköhler (1940) proposed a linear relation between S_T/S_L and u'/S_L for 'large-scale turbulence' (small u'/S_L). Pocheau (1992) later showed that a power law of the form $S_T/S_L = (1 + (u'/S_L)^n)^{1/n}$ satisfies scale invariance in the corrugated flame limit. A spectral closure of the level-set equation led Peters (1999) to propose an algebraic equation for the normalized burning velocity in terms of the ratios of both length and velocity scales. More recently, Kolla, Rogerson & Swaminathan (2010) also proposed an algebraic model for the burning rates based on the closure of terms in the Reynolds averaged Navier–Stokes (RANS) equation for the scalar dissipation rate of the progress variable.

Recent theoretical, experimental and numerical studies support the notion that the burning rate depends on the Reynolds number, although not necessarily uniquely on it. Kobayashi *et al.* (1996, 2005) measured mean burning rates in pressurized Bunsen burners equipped with turbulence-generating grids, finding increasing values of S_T/S_L for increasing pressures at constant values of u'/S_L. When u'/S_L was held constant alongside the geometry of the burner and grids, giving a nearly constant integral scale l also, the increase in S_T/S_L correlates with the increase in Reynolds number brought by the decreasing kinematic viscosity with increasing pressure. Experiments of turbulent spherical premixed flames at the University of Leeds postulated and explored the dependence of S_T/S_L on $Re \sim u'l$ or $Re_\lambda \sim u'\lambda$ (Andrews, Bradley & Lwakabamba 1975; Abdel-Gayed & Bradley 1977; Abdel-Gayed, Bradley & Gray 1981), where λ is the transverse Taylor micro-scale (Taylor 1935).

Starting from the spectral closure of the level-set equation (Peters 1992), Chaudhuri, Akkerman & Law (2011) proposed and later confirmed experimentally (Chaudhuri *et al.* 2012) a $Re^{1/2}$ scaling for S_T/S_L in turbulent spherical premixed flames, where Re is based on the turbulent flame radius and the reactants' thermal diffusivity. Subsequent experimental evidence corroborating the $Re^{1/2}$ scaling includes measurements for a variety of reactive mixtures, pressures and turbulence parameters (Chaudhuri, Wu & Law 2013; Wu *et al.* 2015; Jiang *et al.* 2016). Some universality of the proposed scaling was also demonstrated by collapsing the data from Kobayashi *et al.* (1996, 2005).

Liu *et al.* (2012) investigated the dependence of turbulent flame speeds in pressurized premixed methane/air mixtures propagating in homogeneous isotropic turbulence up to $Re_\lambda \approx 100$. By controlling independently u' and l (via fan speed) and the reactants' kinematic viscosity ν (via pressure), the authors were able to measure burning rates for various values of u'/S_L, while holding Re_λ constant and experiments were repeated for several values of the Reynolds number. The turbulent flame speed S_T/S_L was found to increase with Reynolds number, remaining nearly constant as u'/S_L varied at constant Reynolds number. Ahmed & Swaminathan (2013, 2014) also reported $S_T/S_L \sim Re_T^{0.55}$

based on unsteady RANS simulations of methane/air and hydrogen/air flames, where $Re_T = u'l/\nu$ is the turbulent Reynolds number.

In this study we investigate the Reynolds dependence of burning rates of spherical turbulent premixed flames in decaying isotropic turbulence with direct numerical simulations (DNS). The simulations are conducted at increasing Reynolds number and low values of the Karlovitz number, so that turbulent combustion occurs in the flamelet limit (Libby & Bray 1980; Libby & Williams 1994; Peters 2000), where modifications to flame propagation are negligible.

The statistical state of turbulence encountered by the propagating flame is characterized solely by the velocity fluctuation u', integral length scale l and kinematic viscosity ν. Statistics are a function of time and radial distance from the centre of the spherical flame only, so that ensemble averages are gathered over the polar and azimuthal angles at each instant in time.

Freely decaying isotropic turbulence was preferred to forced turbulence for this study due to the following considerations. Firstly, it is representative of many real devices in which turbulence decays spatially, such as in jets; or temporally, such as in an internal combustion engine. Secondly, decaying isotropic turbulence is well understood through a vast literature (Batchelor & Townsend 1948*a*; Baines & Peterson 1951; Comte-Bellot & Corrsin 1971; Huang & Leonard 1995), which allows us to identify and compensate transient effects consistently across simulations with varying Reynolds number and turbulence scales. We find the opportunity to compare against known results in decaying turbulence preferable to introducing a forcing term in the momentum equation as commonly done in isothermal flows, since theoretical results on forced variable density flows do not exist to our knowledge.

The rest of the article is organized as follows. Section 2 describes the governing equations and numerical methods. The configuration is presented in § 3. The temporal evolution of integral properties of the turbulent flames, such as burning rates, flame radius and flame surface area are discussed in § 4. Section 5 presents the analysis of the evolution of the peak surface density function and turbulent flame brush thickness. Scaling laws are proposed for both quantities separately in § 6 and a scaling law for the evolution of the flame area ratio as a function of the Reynolds number is discussed. The article concludes in § 7 with a summary of the results and prominent findings.

2. Governing equations

The evolution of the flow is described by the reactive multi-component Navier–Stokes equations in the low Mach number limit (Tomboulides, Lee & Orszag 1997; Mueller 1999). The continuity and momentum equations read as

$$\frac{\mathrm{D}\rho}{\mathrm{D}t} = -\rho \nabla \cdot \boldsymbol{u} \tag{2.1}$$

and

$$\rho \frac{\mathrm{D}\boldsymbol{u}}{\mathrm{D}t} = -\nabla \pi + \nabla \cdot \boldsymbol{T}, \tag{2.2}$$

respectively. Here $\mathrm{D}/\mathrm{D}t = \partial/\partial t + \boldsymbol{u} \cdot \nabla$ denotes the material derivative, where $\boldsymbol{u}$ is the mass averaged bulk velocity (Bird, Stewart & Lightfoot 2006). In the momentum equation, $\boldsymbol{T}$ is the viscous shear stress tensor and $\pi = \pi(\boldsymbol{x}, t)$ is the hydrodynamic pressure, which is

small compared to the spatially homogeneous background thermodynamic pressure $p = p(t)$. The mixture density ρ obeys the equation of state for a mixture of ideal gases

$$p = \rho \mathcal{R} T / W, \tag{2.3}$$

where $\mathcal{R}$ is the universal gas constant and W the molar mass of the mixture and T is temperature. Thus, spatial variations in density are related to spatial variations in temperature and mixture composition, but not in pressure.

A Newtonian fluid model is used for closure of the viscous shear stress tensor

$$\boldsymbol{T} = \mu \left(\boldsymbol{\nabla u} + (\boldsymbol{\nabla u})^{\mathrm{T}} \right) - \tfrac{2}{3} \mu (\boldsymbol{\nabla} \cdot \boldsymbol{u}) \boldsymbol{I}, \tag{2.4}$$

where $\boldsymbol{\nabla u}$ is the velocity gradient tensor and $\boldsymbol{I}$ is the identity tensor. A mixture-averaged model is employed for the dynamic viscosity of the mixture μ (Wilke 1950; Bird *et al.* 2006).

The species densities are $\rho_i = \rho Y_i$, where Y_i is the mass fraction of the i-th species, and obey the following transport equations ($i = 1, \ldots, M$):

$$\rho \frac{\mathrm{D} Y_i}{\mathrm{D} t} = -\boldsymbol{\nabla} \cdot (\rho_i \boldsymbol{V}_i) + \omega_i. \tag{2.5}$$

Here ω_i and $\boldsymbol{V}_i$ refer to the net rate of production of species i due to chemical reactions and the mass diffusion velocity, respectively. Diffusive transport of species is modelled with the Hirschfelder–Curtiss approximation (Hirschfelder *et al.* 1954; Poinsot & Veynante 2012)

$$\boldsymbol{V}_i X_i = -\mathcal{D}_i \boldsymbol{\nabla} X_i, \tag{2.6}$$

where

$$\mathcal{D}_i = (1 - Y_i) \Bigg/ \left(\sum_{\substack{j=1 \\ j \neq i}}^{M} X_j / \mathcal{D}_{ij} \right). \tag{2.7}$$

We denote by X_i the mole fraction of the i-th species. In the above equations, $\mathcal{D}_{ij}$ and $\mathcal{D}_i$ are the binary and species diffusion coefficients, respectively. Closure for the mass diffusion velocity reads as

$$\rho_i \boldsymbol{V}_i = -\rho \mathcal{D}_i \frac{Y_i}{X_i} \boldsymbol{\nabla} X_i = -\rho \mathcal{D}_i \frac{\boldsymbol{\nabla} (W Y_i)}{W}. \tag{2.8}$$

This approximation is complemented by a small correction velocity $\boldsymbol{u}^c$ in order to ensure total mass conservation, yielding

$$\frac{\partial \rho_i}{\partial t} + \boldsymbol{\nabla} \cdot (\rho_i (\boldsymbol{u} + \boldsymbol{u}^c)) = -\boldsymbol{\nabla} \cdot (\rho_i \boldsymbol{V}_i) + \omega_i, \tag{2.9}$$

where

$$\boldsymbol{u}^c = -\sum_{i=1}^{M} Y_i \boldsymbol{V}_i = \sum_{i=1}^{M} \mathcal{D}_i Y_i \frac{\boldsymbol{\nabla} W}{W} + \sum_{i=1}^{M} \mathcal{D}_i \boldsymbol{\nabla} Y_i. \tag{2.10}$$

The equation for the conservation of enthalpy is manipulated into a differential equation for temperature:

$$\rho c_p \frac{\mathrm{D}T}{\mathrm{D}t} = \frac{\mathrm{d}p}{\mathrm{d}t} + \nabla \cdot (\Lambda \nabla T) - \sum_{i=1}^{M} c_{p,i} \rho_i V_i \cdot \nabla T - \sum_{i=1}^{M} h_i \omega_i. \tag{2.11}$$

The equation above assumes that viscous heating is negligible on account of the low speed of the fluid and the fact that the pressure field p is spatially homogeneous, albeit varying in time. A mixture-averaged model is employed for the thermal conductivity Λ (Mathur, Tondon & Saxena 1967). The specific enthalpy and the specific heat at constant pressure for species i are $h_i = h_i(T)$ and $c_{p,i} = c_{p,i}(T)$, respectively, and are evaluated from NASA tables (McBride, Gordon & Reno 1993).

Closure for the source terms ω_i is provided by a skeletal chemical kinetics mechanism featuring 16 species and 73 elementary reactions of the Arrhenius type, obtained from GRI-mech 3.0 (Smith *et al.* 1999). The use of a skeletal kinetics mechanism reduces computational costs while modelling key properties accurately, such as ignition delay time, laminar flame speed and thickness. More details on the kinetics mechanism and a comprehensive suite of validation cases are given in Luca *et al.* (2018*a*).

The configuration is a closed vessel of constant volume V, so that the evolution of the background pressure $p(t)$ is obtained from the conservation of mass in the vessel,

$$p = \left(\int_V \frac{W}{T} \, \mathrm{d}V \right)^{-1} m\mathcal{R}, \tag{2.12}$$

where m is the constant mass in the domain.

2.1. *Numerical methods*

Equations (2.1), (2.2), (2.5) and (2.11) are integrated in time with the finite difference solver 'NGA' on a homogeneous Cartesian grid (Desjardins *et al.* 2008). The convective and viscous terms in the momentum equation and the diffusive terms in the scalar equations are discretized with second-order centred finite difference formulas on a staggered grid. The third-order weighted essentially non-oscillatory scheme (Liu, Osher & Chan 1994) is used for the convective terms in the scalar transport equations. Mass conservation is enforced by solving a Poisson equation for the hydrodynamic pressure π instead of the continuity equation. The discrete form of the pressure equation is obtained with centred second-order finite difference formulas.

The advancement in time of the governing equations follows a splitting approach (Pierce 2001). The momentum and pressure equations are coupled with the classic pressure-correction method (Chorin 1968). The momentum equation is integrated in time with a semi-implicit method featuring the explicit second-order Adams–Bashforth method for the convective terms and the implicit Crank–Nicolson method for the linear viscous terms (Kim & Moin 1985). The linear system ensuing from the viscous terms is solved in factored form with the alternating direction implicit (ADI) method (Peaceman & Rachford 1955). The time advancement of the temperature and mass fractions is performed with a first-order Lie splitting approach, whereby the integration of the convective and diffusive terms is performed first for each scalar field independently and that of the reactive source terms is handled at each grid point next. The temporal integration of the convective and diffusive terms is semi-implicit with the convective terms treated explicitly and the linear diffusive terms with the implicit Crank–Nicolson method and ADI factorization.

The integration of the reactive source terms is performed pointwise with adaptive backward differentiation formula methods as implemented in the CVODE solver for systems of ordinary differential equations (Hindmarsh *et al.* 2005).

The variable coefficients pressure equation is solved with the library HYPRE (Falgout, Jones & Yang 2006) using the preconditioned conjugate gradient iterative solver coupled with the parallel alternating semi-coarsening multi-grid V-cycle preconditioner. All governing equations are coupled together with an outer iteration loop and convergence is found to be adequate after two iterations (Pierce 2001).

The grid is homogeneous and isotropic with spacing $\Delta = 20$ μm and the time step size is constant at $\Delta t = 0.2$ μs. The spatial and temporal resolutions are adequate, since $\eta/\Delta \geqslant 0.5$ and $\tau_\eta/\Delta t \geqslant 20$, where η and τ_η are the Kolmogorov length and time scale, respectively. Moreover, $\delta_L/\Delta \geqslant 6$, where δ_L is the thermal thickness of the flame, as defined later in § 3. Extensive numerical tests to confirm adequate spatial resolution for the reactive fronts were carried out for turbulent premixed jet flames (Luca *et al.* 2018*b*) and are not repeated here.

3. Flow configuration

The configuration consists of a cubic box filled with a reactive mixture and initialized with homogeneous isotropic turbulence. A spherical kernel of burnt gases is initialized at the centre of the domain and a turbulent flame propagates outward into freely decaying turbulence. Periodic boundary conditions are imposed in all three directions, so that the computational domain represents a closed vessel. As burnt gases are produced behind the flame, the background pressure increases and the mixture is compressed isentropically. A schematic of the configuration is shown in figure 1.

The reactants are a fully premixed mixture of methane and air with equivalence ratio 0.7. At the onset of the simulation, the temperature and pressure are 800 K and 4 atm, respectively. At these thermo-chemical conditions, the laminar flame speed is $S_L = 1$ m s^{-1}, the thermal thickness is $\delta_L = (T_b - T_u)/max\{|\nabla T|\} = 0.11$ mm and the characteristic flame time $\tau_L = \delta_L/S_L = 0.11$ ms. Here, T_b and T_u are the temperatures of the products and reactants, respectively, and $max\{|\nabla T|\}$ is the maximum value of the temperature gradient across the laminar flame.

In this study a set of three primary simulations, denoted by $R1$, $R2$ and $R3$, are performed at increasing Reynolds number (see table 1). The Reynolds number is adjusted by varying the initial values of the fluctuation u' and integral scale l. Thus, the initial Reynolds number increases due to both u' and l increasing from $R1$ to $R3$. On the other hand, the Kolmogorov length scale η, velocity scale u_η and time scale τ_η are unchanged. Since the reactive mixture and associated flame scales S_L, δ_L and τ_L are unchanged also, this results in a constant initial Karlovitz number $Ka = \tau_L/\tau_\eta = 25$ for all three simulations.

Turbulence decays freely as the flame front moves from the centre outwards. The statistical state of turbulence encountered by the propagating flame is characterized solely by the velocity fluctuation u', integral length scale $l = u'^3/\epsilon$ based on the mean dissipation rate ϵ of the turbulent kinetic energy k, and kinematic viscosity ν, which all evolve in time. The eddy turnover time $\tau = k/\epsilon$ is taken to represent a characteristic time for the motion of the largest scales. The relevant Reynolds number characterizing turbulence is $Re_\lambda = u'\lambda/\nu$, based on the transverse Taylor micro-scale $\lambda^2 = 15\nu u'^2/\epsilon$.

All characteristic scales of turbulence are evaluated with samples gathered in the volume occupied by the reactants only. Fluctuations are evaluated by subtracting the mean from the instantaneous field and the mean is obtained by averaging along spherical shells as

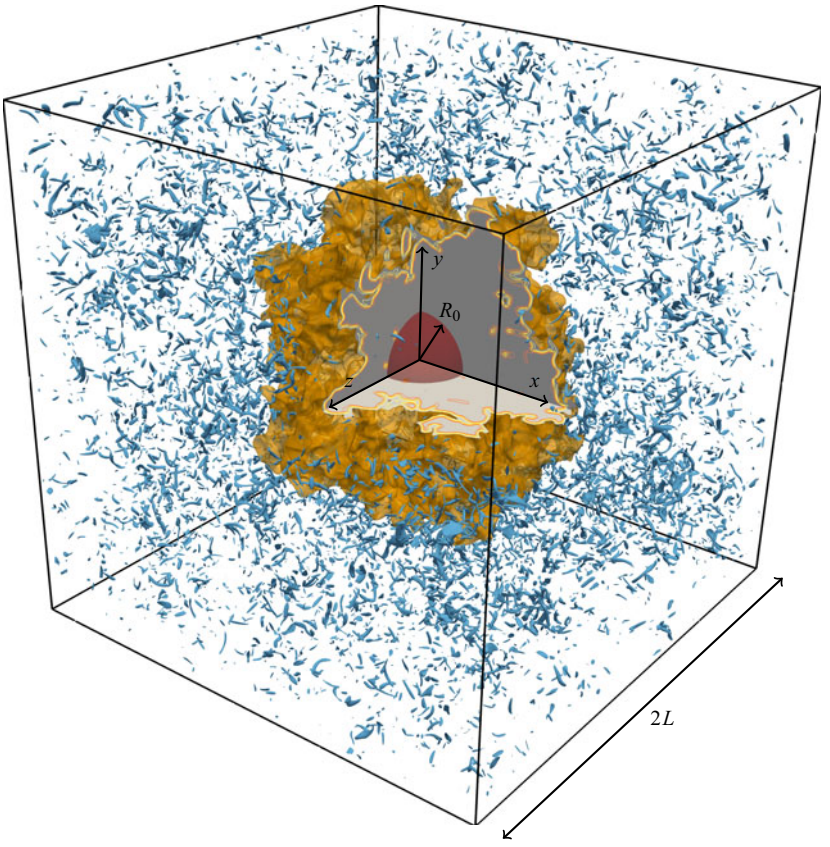

FIGURE 1. Turbulent spherical premixed flame in a cubic box of side $2L$ with periodic boundary conditions. The instantaneous flame surface (orange colour) is surrounded by homogeneous isotropic turbulence, represented by isosurfaces of vorticity (blue colour). The flame surface corresponds to an isosurface of the progress variable. The kernel of burnt gases at the onset of the simulation is shown as a sphere of radius R_0 in the cut-out (red colour).

Simulation	N	$2R_L/l_0$	$2R_0/l_0$	R_L/R_0	u'_0/S_L	l_0/δ_L	δ_L/η	Re_λ	Ka	τ_0/τ_L
$R1$	512^3	33.8	6.9	4.9	7.4	3.4	11.3	44	25	0.69
$R2$	1024^3	43.8	6.7	6.5	8.5	5.2	11.3	59	25	0.91
$R3$	2048^3	59.4	6.3	9.4	9.8	7.8	11.5	77	25	1.18
$R3s$	1024^3	29.7	6.3	4.7	9.8	7.8	11.5	77	25	1.18
$R2a$	1024^3	36.7	6.7	5.5	7.4	6.3	9.65	59	18	1.29

TABLE 1. Turbulence parameters at the onset of the simulations. Here N is the number of grid points. The effective domain radius $R_L = 2(3/4\pi)^{1/3}L \approx 1.24L$ is defined based on L, half the length of the side of the cubic domain. The flame properties are $\delta_L = 0.11$ mm, $S_L = 1$ m s^{-1} and $\tau_L = 0.11$ ms. The Karlovitz number is defined as $Ka = \tau_L/\tau_\eta$.

appropriate (see § 4.3). As turbulence decays freely while the flame propagates, the ratios u'/S_L and l/δ_L vary in time, as shown in figure 2. It is apparent that u'/S_L decreases as time progresses, while l/δ_L increases slightly. The Karlovitz number decreases to $Ka \approx 4$.

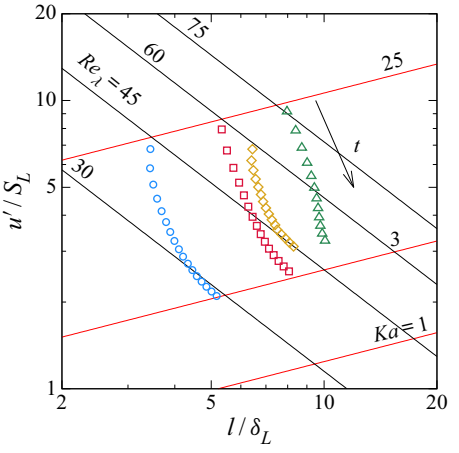

FIGURE 2. Instantaneous values of u'/S_L and l/δ_L on the Borghi–Peters diagram of turbulent premixed combustion (Peters 2000): $R1$ (◯), $R2$ (□), $R2a$ (◇) and $R3$ (△). The arrow points in the direction of increasing time. Also shown are lines of constant $Re_\lambda = u'\lambda/\nu$ and $Ka = \tau_L/\tau_\eta$.

According to the Borghi–Peters classification (Peters 2000), all turbulent premixed flames belong to the flamelet regime.

The computational domain is a cube with side of length $2L$. For reasons that will become clear later, we define the radius of a sphere, whose volume is equal to that of the cubic domain, $R_L = 2(3/4\pi)^{1/3}L \approx 1.24L$. It is apparent from table 1 that the size of the computational domain is large compared to the integral length scale. For example, $2R_L/l \geqslant 30$ across all simulations. In particular, the extent of the domain is much larger than typically required for DNS of isothermal homogeneous isotropic turbulence at the same Reynolds number.

Because the computational domain is large, the extent of the flame's surface may be initialized (and later grow to be) large compared to the integral length scale l. Although a rigorous quantitative definition will be given later in the article, the term 'extent' refers to R, the mean of the surface averaged radial distance of the turbulent flame from the centre of the domain. Since $R \gg l$ throughout the evolution of the flame, the flame is wrinkled by many eddies, the statistics are converged and spherically symmetric, and the flame remains centred in the middle of the domain (see § 4.3).

The fact that the flame is large compared to the integral scale of the flow allows for motions over the entire turbulent spectrum to interact with the surface and affect its evolution. In other words, the entire spectrum of turbulence contributes to flame wrinkling, folding and stretching. As articulated by Chaudhuri *et al.* (2011), if the integral scale were larger than the spherical flame, it is reasonable to expect that the flame's linear extent would act as a cut-off scale, limiting the interaction between the flame and turbulence to those scales smaller than the flame itself.

In keeping with the requirement that the initial flame kernel be large compared to the integral scale, the radius of the spherical kernel of burnt gases at the onset of the simulations R_0 is rescaled to be consistent with l, so that the ratio $2R_0/l \approx 7$ remains approximately constant across configurations. On the other hand, the domain size R_L/l varies across simulations, although it is always large as discussed.

Two additional simulations, denoted by $R2a$ and $R3s$, were conducted. Simulation $R2a$ features the same initial Reynolds number as $R2$, but the fluctuation u' is lower, matching

that of $R1$ and lowering the Karlovitz number. Comparisons between $R1$, $R2a$ and $R2$ explore the dependence of the turbulent burning rates on u'/S_L, l/δ_L and Re_λ. Moreover, in order to investigate the effect of domain size on the propagation of the turbulent spherical premixed flame, simulation $R3$ was repeated with a domain of half the size and labelled $R3s$. Simulation $R3s$ showed that the domain size R_L/l does not have any noticeable affect on the statistics pertaining to the evolution of the flame surface, although the size does affect the mean radial velocity induced by combustion (see § 4.3).

3.1. *Initial conditions and turbulence decay*

The initial homogeneous isotropic turbulence (HIT) is generated as follows. First, preliminary HIT simulations at the target Re_λ are performed with the linear forcing scheme of Rosales & Meneveau (2005). Second, the velocity and dimensions are scaled to obtain the desired values of u' and l and several independent realizations of the velocity field are patched together into a larger domain. The motivation for patching boxes of homogeneous isotropic turbulence, rather than simulating fluid flow in the larger box, is due to a well-known outcome of the forcing scheme, i.e. when a statistically stationary state is attained, the integral scale l is approximately 20 % of the side of the cubic domain. Discontinuities in the velocity field across patches disappeared upon advancing the state over $2\tau_\eta$.

This patching strategy does not compromise the evolution of turbulence during decay as shown by previous studies (Albin 2010; Albin & D'Angelo 2012) and all turbulence statistics are consistent with the theory of decaying turbulence. In particular, the decay of the turbulent kinetic energy follows the power law (Batchelor & Townsend 1948*a*,*b*; Sinhuber, Bodenschatz & Bewley 2015),

$$k/k_0 = (1 + t/t_0)^{-n}, \tag{3.1}$$

where t_0 is the virtual origin, k_0 the turbulent kinetic energy at $t = 0$ and n is the decay exponent.

Experimentally, n is found to lie between 1 and 1.5. For decaying turbulence behind passive grids, Batchelor & Townsend (1948*a*) find $n = 1$, Comte-Bellot & Corrsin (1971) report $1.16 \leqslant n \leqslant 1.37$, while Baines & Peterson (1951) find a higher value of $n = 1.43$. Mohamed & Larue (1990) report that $n = 1.25$ fitted their data best. Here, instead of fitting the parameters in (3.1) directly, we use the expression for the eddy turnover time

$$\tau = k/\epsilon = t_0/n(1 + t/t_0) = t_0/n + t/n, \tag{3.2}$$

so that n and $t_0 = n\tau_0$ are related to the slope and intercept of a least-squares fit to $\tau(t)$.

Figure 3(*a*) shows fits and power laws for k/k_0 and ϵ/ϵ_0. In all simulations we find $n = 1.55$, which is slightly higher than the values reported in the literature. This discrepancy may be due to the low Reynolds number of our configurations or the dependence of the exponent on geometry, which differs between grid generated turbulence and simulations of homogeneous isotropic decaying turbulence.

Figure 3(*b*) compares the decay of Reynolds number in reactive and isothermal simulations from the same initial conditions. Statistics in the isothermal simulations are consistent with the power law decay, while in the reactive simulations, the changes in the background pressure and temperature cause minor deviations. While higher pressure and temperature lead to modifications to the density and the viscosity of the mixture, they are minor on the account of the fact that the maximum pressure rise is less than 20 % across all simulations. Further, the differences at the end of the simulations are due in part

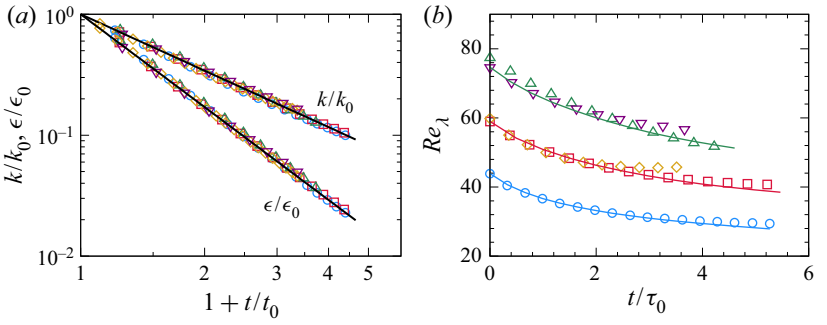

FIGURE 3. Statistics of the decaying turbulence in the reactants. (*a*) Exponential decay of turbulent kinetic energy k/k_0 and its mean rate of dissipation ϵ/ϵ_0 versus $1 + t/t_0$, where $t_0 = n\tau_0$. Lines represent power law expressions with $n = 1.55$. (*b*) Evolution of $Re_\lambda = u'\lambda/\nu$. Lines represent decay in isothermal simulations, symbols represent data from reactive simulations: *R*1 (◯), *R*2 (□), *R*2*a* (◇), *R*3 (△) and *R*3*s* (▽).

to a decreasing number of samples available for statistics, since the reactants occupy a region that decreases in volume as time progresses. We conclude that, apart from minor differences that become more apparent at later times, the presence of a propagating flame does not change the decay of turbulence.

Finally, we notice that the data for simulations *R*3 and *R*3*s* prove that changes in the domain size do not have any noticeable effect on the statistics of decaying turbulence with or without a propagating flame.

4. Overview of the evolution of the turbulent premixed flames

4.1. *Basic definitions*

Within the scope of the present study, the flame surface corresponds to an isosurface of the reaction progress variable $C(\boldsymbol{x}, t) = c^*$, which is defined as

$$C = 1 - \frac{Y_{O_2} - Y^b_{O_2}}{Y^u_{O_2} - Y^b_{O_2}}, \tag{4.1}$$

where Y_{O_2} is the mass fraction of molecular oxygen and $Y^u_{O_2}$ and $Y^b_{O_2}$ are the mass fraction of oxygen in the reactants and products, respectively. We let the iso-level $c^* = 0.73$ define the flame surface. This particular value of the progress variable corresponds to the maximum value of the heat release rate, which is taken to mark the middle of the reaction zone. The normal to the flame surface is $\boldsymbol{n} = -\nabla C/|\nabla C|$, such that it points into the reactants. The flame propagates in the direction of the normal with a displacement speed S relative to the local fluid velocity, given by (Pope 1988; Chakraborty & Cant 2005)

$$S = \frac{1}{|\nabla C|}\frac{\mathrm{D}C}{\mathrm{D}t} = \frac{1}{|\nabla C|}\left(\frac{\partial C}{\partial t} + \boldsymbol{u}\cdot\nabla C\right). \tag{4.2}$$

The displacement speed is calculated from the progress variable field as follows. The temporal derivative $\partial C/\partial t$ is computed at the intermediate time $t_{1/2} = t_n + \Delta t/2$ with a central finite difference formula based on two solutions at t_n and $t_{n+1} = t_n + \Delta t$. The velocity and scalar fields are interpolated linearly in time to $t_{1/2}$, the staggered velocity

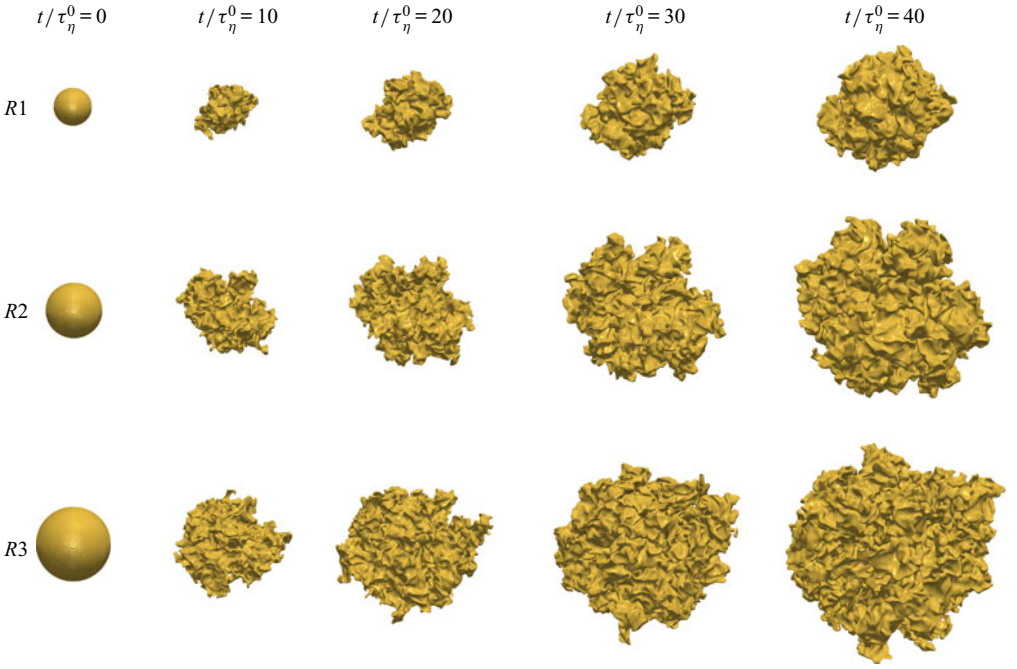

FIGURE 4. Instantaneous flame surface shown at various dimensionless times for the simulations $R1$, $R2$ and $R3$. The Reynolds number increases from top to bottom, while the simulation time increases from left to right. Since τ_η^0 is the same for all three simulations, the flame surface is compared at the same physical time across simulations. The physical dimension is the same for all three flames also.

components are interpolated linearly onto the centred grid used for the progress variable scalar field, and a high-order central finite difference formula is used to evaluate the gradient of C.

The displacement speed is calculated based on the material derivative instead of the sum of the reactive and diffusive terms for the sake of computational convenience. The use of mixture-averaged diffusion models make the numerical evaluation of the diffusive term cumbersome. Also, the operator splitting approach coupled with the semi-implicit time advancement leads to the evaluation of the reactive and diffusive terms at different physical times, leading to ambiguity. Conversely, the solution field $C(\boldsymbol{x}, t)$ is accurate to the method's order at each discrete time step.

4.2. *The evolution of the turbulent premixed flames*

Figure 4 illustrates the evolution of the turbulent spherical premixed flame during simulations $R1$, $R2$ and $R3$. The surface of the flame is visualized by the isosurface $C(\boldsymbol{x}, t) = c^*$, which marks the thin reaction zone of the flame. The flame, which is initialized as a spherical kernel of products centred in the middle of the computational domain, propagates radially outwards into the premixed reactants. Movies of the propagating flames are provided in the supplementary material available at https://doi.org/10.1017/jfm.2020.784.

It is apparent that the flame surface is wrinkled and folded by turbulence as the flame propagates. Most patches of the flame surface are flat or posses only a slight curvature.

Regions of high curvature are much less prevalent and appear as sharp cylindrical folds, while cusps are infrequent. These qualitative observations are consistent with established topological features of the surface of turbulent premixed flames (Cifuentes *et al.* 2014). If the flames are compared at times when they are of similar size, the flame at the greatest value of the Reynolds number ($R3$) displays the highest density of folds and wrinkles. This is consistent with the qualitative interpretation that scale separation increases with increasing Reynolds number.

As reactants are converted into products inside the closed domain, the background pressure increases, leading to an increase in the reactants' temperature T_u also. The compression is isentropic. The simulations terminate when the mass fraction of burnt gases is less than 25 % of the total, such that the effect of periodic boundary conditions is negligible. This ensures a small change in T_u ($\leqslant 3\,\%$) and p ($\leqslant 20\,\%$) for all simulations. Such small changes in pressure and temperature lead to negligible changes in the laminar flame speed S_L ($\leqslant 1\,\%$) and flame thickness δ_L ($\leqslant 10\,\%$).

4.3. *Mean velocity field*

The statistical analysis that follows assumes flow ergodicity in the polar and azimuthal coordinates, allowing to gather samples on spherical shells from one simulation. Indeed, one expects that the statistics of the flame surface are spherically symmetric far from the periodic boundaries. Verification of such symmetry is thus critical to the analysis and is explored here briefly for the mean velocity field.

Away from the flame brush, the density field is homogeneous and the general solution of the Reynolds averaged continuity equation for a closed domain reads as

$$\langle u_r \rangle = -\frac{1}{3\gamma}\frac{1}{p}\frac{\mathrm{d}p}{\mathrm{d}t}r + C_1 r^{-2}, \tag{4.3}$$

where $u_r = \boldsymbol{u}\cdot\boldsymbol{e}_r$ is the radial component of velocity and C_1 is a constant. The first term in the equation above arises from the evolution of the reactants' and products' densities due to compression, which is found to be isentropic. In the region occupied by products, $C_1 = 0$ since $\langle u_r \rangle = 0$ at $r = 0$, yielding

$$\langle u_r \rangle = -\frac{1}{3\gamma_b}\frac{1}{p}\frac{\mathrm{d}p}{\mathrm{d}t}r, \tag{4.4}$$

where γ_b is the ratio of specific heats of the burnt gases. Equation (4.4) shows that $\langle u_r \rangle$ is negative ($\mathrm{d}p/\mathrm{d}t > 0$) and varies linearly with r in the burnt gases.

At the domain boundary, the velocity is zero due to periodicity, but the boundaries' radial location depends on the polar and azimuthal coordinates on the account of the domain being a cube. Yet, since the mean radial velocity decreases as $1/r^2$, one expects the effect of geometry on the radial velocity to be negligible away from the boundary. Consequently, boundary conditions are imposed at an effective radial distance R_L, defined as the radius of a sphere with volume equal to that of the cubic domain

$$R_L = 2(3/4\pi)^{1/3}L. \tag{4.5}$$

Then, the mean radial velocity component in the reactants reads as

$$\langle u_r \rangle = -\frac{R_L}{3\gamma_u}\frac{1}{p}\frac{\mathrm{d}p}{\mathrm{d}t}\left[\frac{r}{R_L} - \left(\frac{r}{R_L}\right)^{-2}\right], \tag{4.6}$$

where γ_u is the ratio of specific heats of the reactants.

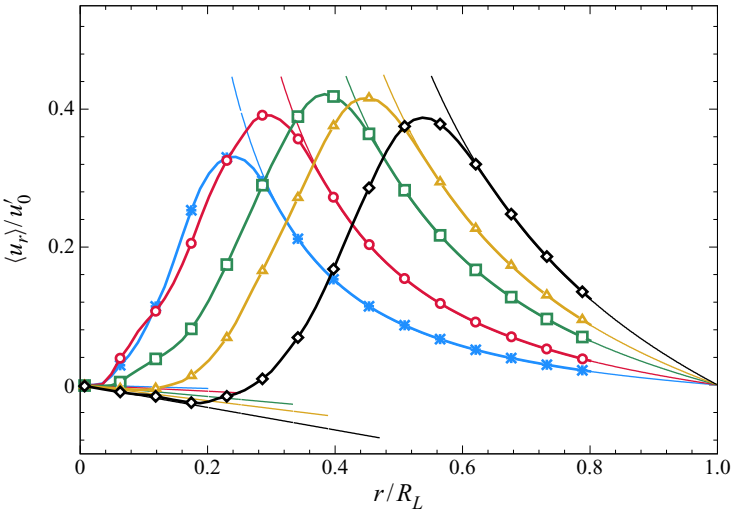

FIGURE 5. Reynolds averaged radial velocity $\langle u_r \rangle$ normalized by the initial turbulence intensity for simulation $R2$. Data at five times: $t/\tau_0 = 1.50$ (∗), 2.23 (◯), 3.35 (□), 4.10 (△) and 5.20 (♢). Thin lines represent the expressions in (4.4) and (4.6) evaluated with the instantaneous value of $p^{-1}\mathrm{d}p/\mathrm{d}t$. Data for $r/R_L \leqslant 0.8$ ($r/L \leqslant 1$), which corresponds to the minimum distance from the centre to the boundary.

Figure 5 shows $\langle u_r \rangle$ at five instants in time during the $R2$ simulation. The mean is obtained by averaging over Θ and Φ. The mean radial velocity matches the expressions in (4.6) and (4.6) closely at radial locations occupied by either products or reactants and away from the brush. In particular, on the reactants' side, the theoretical expression for $\langle u_r \rangle$ is identical to the data from the simulation up to $r/L = 1.0$ (or $r/R_L = 0.8$), which corresponds to the minimum distance between the centre and the faces of the cubic domain. We conclude that the mean flow retains spherical symmetry as if the computational domain were a spherical vessel with radius R_L.

The peak mean radial velocity within the brush increases at first. As the flame grows in size, boundary conditions cause the peak mean radial velocity to decrease due to confinement effects. The evolution of the peak mean radial velocity is qualitatively similar to that of the mean radial velocity at the leading edge of the brush, where (4.6) is applicable. While $1/p\,\mathrm{d}p/\mathrm{d}t$ increases continuously in time, the term inside the square brackets decreases as R/R_L increases and the product of the two is non-monotonic giving rise to the behaviour in figure 5. This conclusion is supported further by the observation that the peak mean radial velocity increases continuously for case $R3$, whereas it shows a non-monotonic behaviour for case $R3s$, which has a domain of half the size (not shown).

In the remainder of this article, turbulent statistics are assumed to be spherically symmetric and statistics are gathered accordingly.

5. Turbulent burning velocity, area ratio and correction factor

The relation between the flame's area and the fuel burning rate is of paramount importance to the understanding of the role of scale separation in turbulent premixed combustion applications.

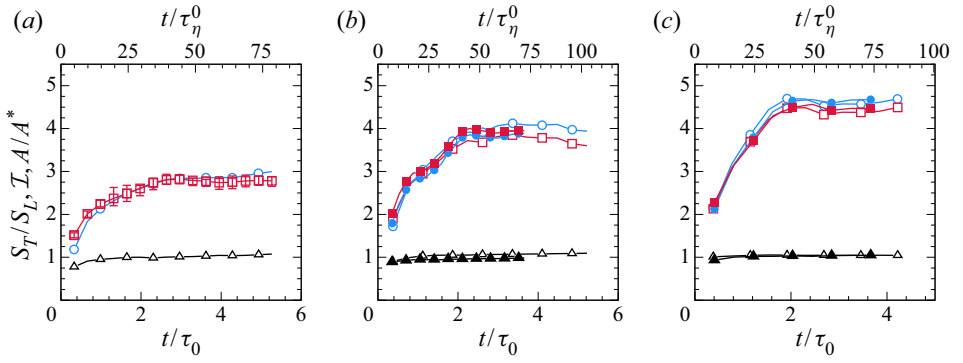

FIGURE 6. Dimensionless turbulent burning velocity S_T/S_L (◯), area ratio χ (□) and correction factor $\mathcal{I}$ (△). (*a*) *R*1 with error bars for the area ratio χ representing the variation across four simulations, (*b*) *R*2 (open symbols) and *R*2*a* (filled symbols) and (*c*) *R*3 (open symbols) and *R*3*s* (filled symbols).

The dimensionless turbulent burning velocity S_T/S_L is defined based on the mean volumetric fuel burning rate Ω_f and a suitable reference area A^*,

$$\frac{S_T}{S_L} = \frac{\Omega_f}{\rho_u Y_f S_L A^*}, \tag{5.1}$$

where ρ_u is the reactants' density and Y_f the mass fraction of the fuel in the reactants.

The mean volumetric fuel burning rate is $\Omega_f(t) \equiv \langle \tilde{\Omega}_f(t) \rangle$, where the brackets indicate statistical expectation and $\tilde{\Omega}_f(t)$ is a random process representing the instantaneous volumetric burning rate at time t. Similarly, we define the mean flame radius $R(t) \equiv \langle \tilde{R}(t) \rangle$, which is referred to simply as flame radius henceforth, and reference area $A^* = 4\pi R^2$. The random process $\tilde{R}(t)$ is the instantaneous surface averaged radial distance of the flame surface from the centre of the domain. Finally, we define the mean of the flame surface area $A(t) \equiv \langle \tilde{A}(t) \rangle$ as the expectation of the random process $\tilde{A}(t)$, which is the instantaneous flame area at time t.

Formal definitions of $\Omega_f(t)$, $R(t)$ and $A(t)$ are provided later in this section, while a comprehensive discussion of the relation between the random processes and their expectations is given in appendix A.

The dimensionless turbulent burning velocity may be written as a product of two quantities as

$$\frac{S_T}{S_L} = \frac{\Omega_f}{\rho_u Y_f S_L A} \frac{A}{A^*} = \mathcal{I}\chi, \tag{5.2}$$

where $\mathcal{I} = \Omega_f/(\rho_u Y_f S_L A)$ is a correction factor and $\chi = A/A^*$ is the area ratio. In the thin reaction zone regime, $\mathcal{I} \approx 1$, $\chi \gg 1$, and the area ratio controls the enhancement of turbulent burning rates as quantified by the dimensionless turbulent burning velocity S_T/S_L.

Figure 6 shows the temporal evolution of S_T/S_L, χ and $\mathcal{I}$ for the five simulations. We observe that the correction factor $\mathcal{I} \approx 1$ as expected. The temporal evolution of the area ratio is qualitatively similar across simulations, in that χ grows rapidly and reaches a plateau afterwards.

When measured in units of eddy turnover time τ_0, the growth in χ lasts approximately $2\tau_0$ for all three simulations. The asymptotic value reached by χ for later times is smallest for $R1$ ($\chi \to 2.8$) and largest for $R3$ ($\chi \to 4.5$). Comparisons across $R3$ and $R3s$ indicate that the size of the domain does not affect the burning rates. As discussed later, the same is observed for all other pertinent statistics.

The comparison of turbulent burning rates from $R1$, $R2$ and $R2a$ points to the role of the Reynolds number in controlling turbulent burning rates. Simulations $R1$ and $R2a$ feature the same turbulence intensity u'/S_L, and yet $R2a$ features higher burning rates than $R1$. On the other hand, simulations $R2$ and $R2a$ share the same Reynolds number, differing in both u'/S_L and l/δ_L, yet they feature identical area ratios χ when plotted versus t/τ_0.

In (5.2) and related commentary above, $\Omega_f(t)$, $R(t)$ and $A(t)$ are time dependent expectations of random processes for which suitable estimators must be defined in a manner consistent with the ergodicity of the flow. In this work we adopt the mathematical framework of the flame surface density function (Pope 1988; Vervisch *et al.* 1995), which is the expectation of the flame surface area per unit volume and defined formally as

$$\Sigma(r,t) \equiv \langle |\nabla C| \delta(C - c^*) \rangle, \tag{5.3}$$

where the surface density function Σ only depends on (r, t) due to the spherical symmetry of the statistics of $C(\boldsymbol{x}, t)$ and the norm of its gradient $|\nabla C|$. Then, the mean flame surface area and the flame radius are

$$A(t) = \int_V \Sigma \, \mathrm{d}V = 4\pi \int_0^\infty r^2 \Sigma(r,t) \, \mathrm{d}r, \tag{5.4}$$

$$R(t) = \frac{1}{A(t)} \int_V |\boldsymbol{x}| \Sigma \, \mathrm{d}V = \frac{4\pi}{A(t)} \int_0^\infty r^3 \Sigma(r,t) \, \mathrm{d}r, \tag{5.5}$$

since $|\boldsymbol{x}| = r$. The area ratio χ written in terms of Σ is

$$\chi(t) = \int_0^\infty (r/R)^2 \Sigma(r,t) \, \mathrm{d}r, \tag{5.6}$$

using the definitions of $A(t)$ and $A^*(t) = 4\pi R(t)^2$. The mean volumetric fuel burning rate is

$$\Omega_f(t) = \int_V \langle \dot{\omega}_f(\boldsymbol{x}, t) \rangle \, \mathrm{d}V, \tag{5.7}$$

where $\dot{\omega}_f(\boldsymbol{x}, t)$ is the instantaneous local rate of consumption of fuel per unit volume.

In the present statistically unsteady flow, there are two manners of estimating expectations: ensemble averaging over $\mathcal{N}$ repetitions (each simulation at the same nominal conditions providing independent random fields) and spherical averaging over the polar (Θ) and azimuthal (Φ) angles, which are coordinates over which the random fields are ergodic,

$$\Sigma(r,t) \equiv \langle |\nabla C| \delta(C - c^*) \rangle \approx \langle \langle |\nabla C| \delta(C - c^*) \rangle_{\Theta\Phi} \rangle_{\mathcal{N}}, \tag{5.8}$$

where $\langle \cdot \rangle_{\mathcal{N}}$ denotes ensemble averaging and $\langle \cdot \rangle_{\Theta\Phi}$ denotes spherical averaging, and the $\approx$ sign indicates that the right-hand side of (5.8) is an estimate subject to statistical errors.

It is desirable to repeat each simulation $\mathcal{N}$ times in order to improve statistical convergence. In the present study, we found that $\mathcal{N} = 1$, i.e. one repetition, was sufficient to obtain rather accurate estimates for the expectations on the account that spherical

averages have small variance. This is explained by the fact that the flame radius R is large compared to the integral scale of the flow l by design.

Repeating simulations was computationally prohibitive, except for the $R1$ simulation, where the number of grid points was small enough to afford four repetitions at the same nominal conditions. In the rest of this article, all statistical quantities presented for $R2$, $R2a$ and $R3$ rely on one simulation, while statistics for $R1$ rely on four simulations. A more comprehensive discussion is included in appendix A.

5.1. *Probability density function of radial distance of the flame surface*

The remainder of this paper is concerned with the mechanisms responsible for the evolution of the area ratio A/A^* and its differences and similarities across simulations. Before presenting a model for the area ratio and its scaling, it is useful to associate a probability density function (PDF) to the distance of the flame surface, denoted by $\mathcal{P}_\phi$. Here ϕ is the random variable representing the radial distance of the flame surface from the origin. With this formalism, the mean flame radius R and the thickness of the turbulent brush δ_T can be defined rigorously in terms of the moments of $\mathcal{P}_\phi$ and their governing equations be derived as shown later.

The expectation of the flame surface area inside a sphere of radius φ is

$$A_\varphi = 4\pi \int_0^\varphi r^2 \Sigma(r,t)\,\mathrm{d}r, \tag{5.9}$$

so that the ratio A_φ/A represents the probability $\mathbb{P}(\phi < \varphi)$ and describes the cumulative density function associated with $\mathcal{P}_\phi$. The PDF is obtained by differentiation with respect to the sample space variable φ,

$$\mathcal{P}_\phi(\phi = \varphi; t) = \mathrm{d}(A_\varphi/A)/\mathrm{d}\varphi = 4\pi A^{-1}\varphi^2 \Sigma(r = \varphi, t), \tag{5.10}$$

with support $\varphi \in [0, \infty)$. The mean μ and standard deviation σ of ϕ are the mean radial distance and a scaled flame brush thickness:

$$\mu = \langle\phi\rangle = \int_0^\infty \varphi \mathcal{P}_\phi(\varphi; t)\,\mathrm{d}\varphi = 4\pi A^{-1} \int_0^\infty r^3 \Sigma(r,t)\,\mathrm{d}r \tag{5.11}$$

and

$$\sigma^2 = \langle(\phi - \langle\phi\rangle)^2\rangle = \int_0^\infty (\varphi - \langle\phi\rangle)^2 \mathcal{P}_\phi(\varphi; t)\,\mathrm{d}\varphi = 4\pi A^{-1} \int_0^\infty (r - R)^2 r^2 \Sigma(r,t)\,\mathrm{d}r. \tag{5.12}$$

The flame radius and the turbulent brush thickness are defined based on μ and σ as $R = \mu$ and $\delta_T = \sqrt{2\pi}\sigma$, respectively. The proportionality constant $\sqrt{2\pi}$ is included in the definition of δ_T for consistency with the common definition of the flame brush thickness based on the mean gradient of the progress variable

$$\delta_T = \sqrt{2\pi}\sigma \approx 1/max\{\mathrm{d}\langle C\rangle/\mathrm{d}r\}, \tag{5.13}$$

where $\langle C\rangle(r,t)$ is the mean progress variable and $\mathrm{d}\langle C\rangle/\mathrm{d}r$ its gradient under the hypothesis of spherical symmetry. The two definitions of the brush thickness are equivalent under the assumption that $\mathcal{P}_\phi$ is normally distributed around the mean (e.g. see Chapter 4 in Lipatnikov 2012).

The evolution equation for $\mathcal{P}_\phi$ is derived starting from that for the flame surface density function. The flame surface density function Σ evolves according to (Pope 1988; Trouvé & Poinsot 1994; Vervisch *et al.* 1995)

$$\frac{\partial \Sigma}{\partial t} + \frac{1}{r^2}\frac{\partial}{\partial r}(\langle u_r + Sn_r\rangle_w \Sigma) = \langle K\rangle_w \Sigma, \tag{5.14}$$

where suitable simplifications due to spherical symmetry are made. Here, S is the displacement speed as defined in (4.2) and u_r and n_r represent the radial components of the velocity and normal vectors, respectively. The operator $\langle\cdot\rangle_w$ denotes the gradient weighted or surface average (Pope 1988).

The flame stretch $K = a - 2S\kappa$ contains two contributions: the tangential strain rate $a = -\boldsymbol{n}^T\boldsymbol{\nabla u n} + \boldsymbol{\nabla}\cdot\boldsymbol{u}$ and the curvature-propagation term $-2S\kappa = S\boldsymbol{\nabla}\cdot\boldsymbol{n}$. The tangential strain rate depends only on the velocity field $\boldsymbol{u}$ and the orientation of the velocity gradient tensor $\boldsymbol{\nabla u}$ with respect to the flame normal $\boldsymbol{n}$. The curvature term is non-zero only for surfaces that propagate ($S \neq 0$) in the presence of curvature ($\kappa \neq 0$). In the case of a material surface, $K = a$ and surface stretch is due to tangential strain alone.

The rate of change of A is solely due to the stretch term of (5.14), as the volumetric integrals of the convective and propagation terms on the left-hand side are zero. The logarithmic time rate of change of the area $= (1/A)\,\mathrm{d}A/\mathrm{d}t$ is therefore called the global stretch and denoted by K_G.

In light of (5.10), the rate of change of $\mathcal{P}_\phi$ reads as

$$\partial\mathcal{P}_\phi/\partial t = \left(4\pi r^2/A\right)\left\{\partial\Sigma/\partial t - (\Sigma/A)\,\mathrm{d}A/\mathrm{d}t\right\}. \tag{5.15}$$

Substituting $\partial\Sigma/\partial t$ from (5.14) into (5.15) and simplifying, we obtain the evolution equation for the PDF

$$\partial\mathcal{P}_\phi/\partial t = -\partial/\partial r\left\{\langle u_r + Sn_r\rangle_w \mathcal{P}_\phi\right\} + (\langle K\rangle_w - K_G)\mathcal{P}_\phi. \tag{5.16}$$

5.2. *Characterization of $\mathcal{P}_\phi$ and Σ*

The mathematical framework presented in § 5.1 demonstrates that the mean area A, mean radius R, turbulent flame brush δ_T and area ratio χ are related functionally to the surface density function Σ. Further, (5.10) points to an equivalence between Σ and the probability density function $\mathcal{P}_\phi$.

The temporal evolution of the flame radius and the turbulent flame brush thickness is shown in figure 7.

The onset of a linear growth phase occurs at $t/\tau_0 \approx 1$ for all configurations and the non-dimensional growth rate $R_0^{-1}\tau_0\,\mathrm{d}R/\mathrm{d}t$ differs, being greatest for $R3$ and smallest for $R1$. The flame brush δ_T/l_0 increases monotonically in time across simulations as shown in figure 7(*b*) and similar across simulations, which is a result of the scaling of the flame brush thickness with the integral length scale of the flow as discussed later in § 6.1.

The PDF $\mathcal{P}_\phi$ is closely approximated by a Gaussian distribution. This is demonstrated in figure 8, which shows $\mathcal{P}_\phi$ at four times for three simulations. Here we plot the PDF normalized by σ and against ϑ, a sample space variable of the normalized brush coordinate $\theta = (\phi - \mu)/\sigma$. It is apparent that $\sigma\mathcal{P}_\phi$ is well described by a standard normal distribution $\mathcal{N}(0, 1)$, consistently with previous data reported in the literature for various flame configurations (Lipatnikov & Chomiak 2002). The inset shows that the tails of the PDF are also well approximated by the normal distribution, although the comparison becomes less satisfactory for $|\vartheta| > 2$, possibly due to statistical convergence.

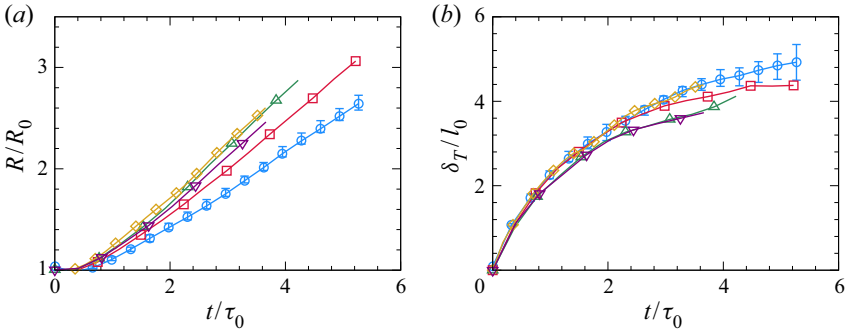

FIGURE 7. Evolution of (*a*) mean flame radius and (*b*) flame brush thickness for various simulations. The mean flame radius is normalized by the initial kernel size R_0, while the brush thickness is normalized with the initial integral length scale l_0: *R*1 (◯), *R*2 (□), *R*2*a* (◇), *R*3 (△) and *R*3*s* (▽). Error bars shown for *R*1 simulation represent the sample variance based on four realizations.

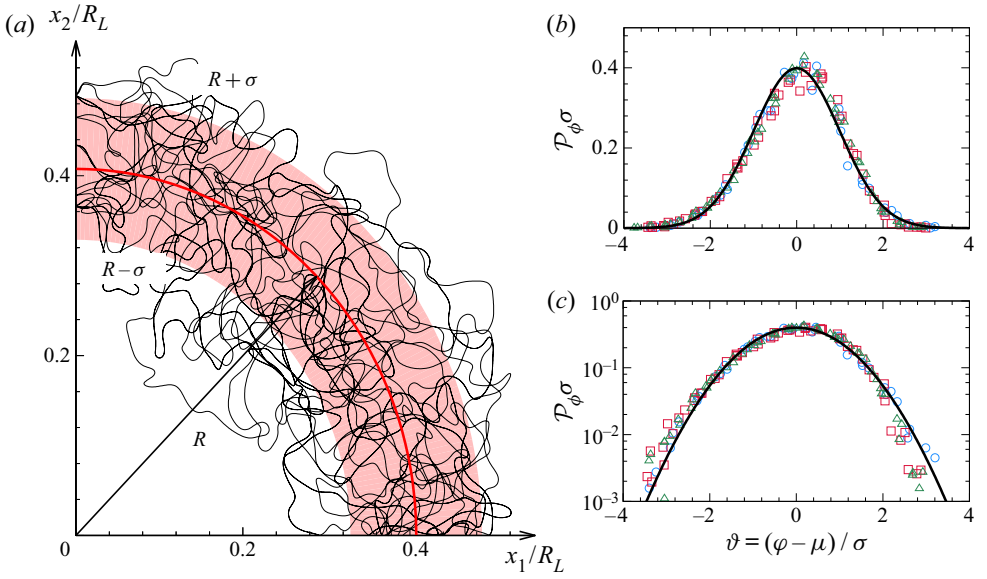

FIGURE 8. (*a*) Representative planar slices of the instantaneous flame surface for simulation *R*2 at $t/\tau_0 = 4.2$. Here x_1–x_2 denotes a quadrant of the Cartesian planes x–y, y–z and x–z. The mean flame radius (thick red line) and several $C = c^*$ isocontours (thin black lines) are shown alongside the shaded region $r = R \pm \sigma$. Also shown in (*b*) and (*c*) is the $\sigma\mathcal{P}_\phi$ at four times for simulations *R*1 (◯), *R*2 (□) and *R*3 (△) with the standard normal distribution for comparison (thick black lines).

Figure 9 shows Σ at select times for simulations *R*1, *R*2, *R*3 and *R*2*a*. The surface density function (SDF) is shown normalized by the initial thermal thickness δ_L^0 and plotted versus r/R_L, where R_L is the effective domain radius (see table 1). The SDF is transported radially outward, broadens, and its maximum value Σ_m decreases with time. This behaviour is common across all cases. The broadening of Σ is consistent with the increase in the flame brush and with experimental observations of spherical turbulent

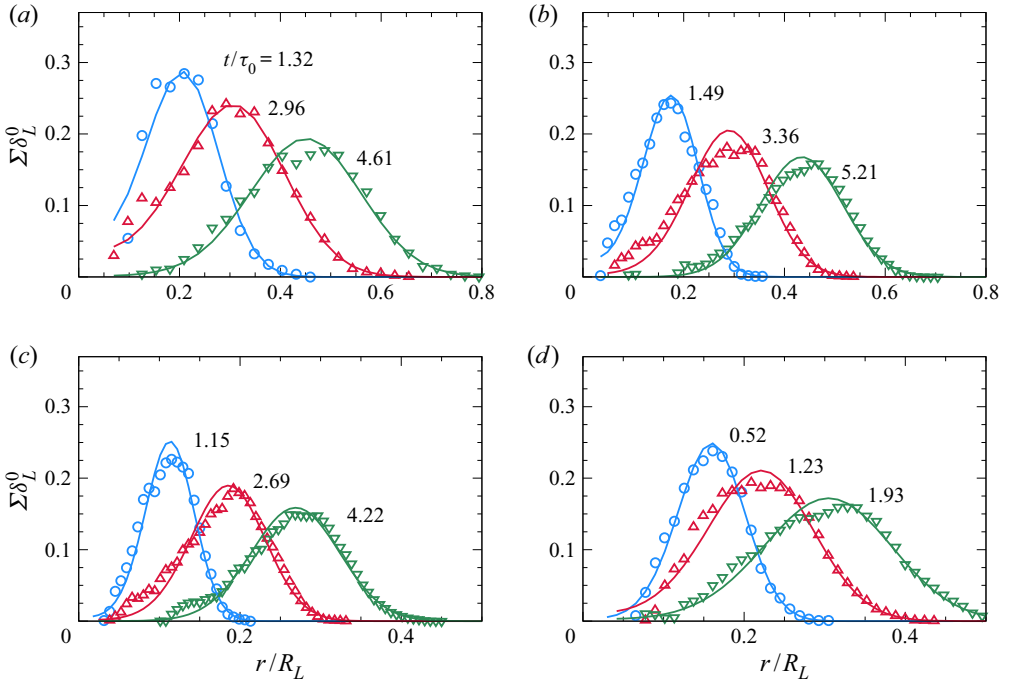

FIGURE 9. Surface density function at select times for (*a*) *R*1, (*b*) *R*2, (*c*) *R*3 and (*d*) *R*2*a*. The normalized time t/τ_0 is shown next to each profile. The surface density distribution broadens and the peak reduces as the time progresses. Symbols denote evaluation of Σ using the definition directly, while solid lines show surface density estimation based on (5.10) and a normal distribution model for $\mathcal{P}_\phi$.

premixed flames evolving in freely decaying turbulence (Renou *et al.* 2002; Fries *et al.* 2019). Since the area ratio χ is related to the volumetric integral of Σ, broadening appears to be closely related to the observed increase of χ in time. Yet, the peak of Σ decreases in time, so that a more quantitative analysis is in order.

Using a Gaussian distribution as a model for $\mathcal{P}_\phi$, the surface density function is obtained according to (5.10) and shown in figure 9 also. The surface density function Σ, obtained assuming that $\mathcal{P}_\phi$ is a normal distribution, is compared to its direct evaluation from the gradient of the progress variable. The comparison is very satisfactory, indicating that the two methodologies are consistent and further validating our approach. Nonetheless, Σ computed from conditional statistics displays residual statistical noise, and, therefore, we rely on the model to analyse the peak value Σ_m of the surface density function.

5.3. *Model for the area ratio*

We begin by noting that the surface density function admits a local maximum at radial location $\hat{r}$, which is the root of the equation

$$\left.\frac{\partial \Sigma}{\partial r}\right|_{r=\hat{r}} = -2\mathcal{P}_\phi(\hat{r})/\hat{r}^3 + \mathcal{P}'_\phi(\hat{r})/\hat{r}^2 = 0, \tag{5.17}$$

$$2\mathcal{P}_\phi(\hat{r}) - \hat{r}\mathcal{P}'_\phi(\hat{r}) = 0, \tag{5.18}$$

where we let $\mathcal{P}'_\phi$ indicate the derivative with respect to φ. Based on (5.10), the maximum value attained by the surface density function is

$$\Sigma_m \equiv \Sigma(\hat{r}, t) = (4\pi)^{-1} A \frac{\mathcal{P}'_\phi(\hat{r})}{2\hat{r}} = (4\pi)^{-1} A \frac{\mathcal{P}_\phi(\hat{r})}{\hat{r}^2}. \tag{5.19}$$

Substitution of (5.10) and (5.19) into (5.6) gives

$$\chi = \Sigma_m \delta_T \beta; \quad \beta = \frac{1}{\mathcal{P}_\phi(\hat{r})\delta_T} \left(\frac{\hat{r}}{R}\right)^2. \tag{5.20a,b}$$

Here β is a shape factor related solely to the functional form of $\mathcal{P}_\phi(\varphi; t)$. Equation (5.20*a*,*b*) illustrates that the area ratio χ is proportional to the product of the maximum value of the surface density function, the thickness of the flame brush and a shape factor.

As shown in figure 8, $\mathcal{P}_\phi(\varphi; t)$ is well approximated by a normal distribution. On the account that $\mathcal{P}_\phi$ is defined in $[0, \infty)$, a truncated normal distribution with parameters $\bar{\mu}$ and $\bar{\sigma}^2$ (Johnson, Kotz & Balakrishnan 1994) is required formally, rather than a normal distribution with infinite support $\varphi \in (-\infty, \infty)$. However, we find that for all simulations, $\bar{\mu} \geqslant 3\bar{\sigma}$ (see figure 8), so that $\bar{\mu} \approx \mu$, $\bar{\sigma}^2 \approx \sigma^2$, and the normalization factor $Z = 1 - F(-\bar{\mu}/\bar{\sigma}) \approx 1$, where $F(z)$ is the cumulative distribution function of the standard normal distribution.

Thus, for all practical purposes, the truncated normal distribution and the underlying normal distribution are identical on the account of the negligible probability of ϕ taking negative values. For simplicity, we ignore the small differences arising from the truncated sample space at $\varphi = 0$ and model $\mathcal{P}_\phi$ as a normal distribution with parameters $\mu = R$ and $\sigma^2 = \delta_T^2/(2\pi)$. This results in the following root of (5.18):

$$\hat{r} = 2\mathcal{P}_\phi(\hat{r})/\mathcal{P}'_\phi(\hat{r}) = R\left(1 + \sqrt{1 - 8\alpha^2}\right)/2. \tag{5.21}$$

Here $\alpha = \sigma/\mu$ ($\alpha \leqslant 0.33$ for all times and simulations) is the relative standard deviation of the radial distance. Substituting (5.21) into (5.20*b*), the shape factor reads as

$$\beta = \beta(\alpha) = 0.25(1 + \sqrt{1 - 8\alpha^2})^2 \exp\left\{\alpha^2(\sqrt{1 - 8\alpha^2} - 1)^2/8\right\}. \tag{5.22}$$

Equation (5.22) indicates that the shape factor is a monotonic function of α. For $\alpha \to 0$, $\beta \to 1$ and decreases as α increases. For all simulations and times, we find that $0.875 \leqslant \beta \leqslant 1$.

Together with the fact that $\beta \approx 1$, (5.20*a*) illustrates that the area ratio χ is equal to the product of the maximum value of the surface density function Σ_m and the thickness of the flame brush δ_T. The temporal evolution of these two quantities across simulations with varying Reynolds number is explored closely in the remainder of the paper.

6. Scaling of the area ratio in spherical turbulent premixed flames

6.1. *Scaling of the turbulent flame brush thickness*

As defined in (5.13), the flame brush thickness $\delta_T(t)$ is a statistical measure of the distance of the flame surface from its mean location. The brush thickness grows from zero as time progresses and turbulence wrinkles the flame (figure 7*b*).

Under rather stringent assumptions and important approximations, Taylor's theory of turbulent diffusion has been applied to the evolution of the flame brush thickness

(Lipatnikov & Chomiak 2002). First, the flame surface is assumed to evolve as a collection of infinitesimal material surface elements and the variance of the distance of the surface elements from their mean location is taken to represent the brush thickness. Second, turbulence is assumed to be homogeneous and isotropic, although not necessarily stationary. Under these assumptions, the rate of change of the variance of the distance is

$$\mathrm{d}\sigma^2/\mathrm{d}t = 2u'(t)\int_0^t u'(p)f_L(p,t)\,\mathrm{d}p, \tag{6.1}$$

where f_L denotes the Lagrangian velocity autocorrelation function and $u'(t)$ is the turbulence intensity at time t. For stationary turbulence, (6.1) is integrated assuming that the autocorrelation function is exponential (Hinze 1975) to give

$$\sigma^2/l^2 = 2\tilde{t}\{1-\tilde{t}^{-1}[1-\exp(-\tilde{t})]\}, \tag{6.2}$$

where $\tilde{t} = t/\tau^\dagger$ and $\tau^\dagger = l/u'$ is a constant reference time scale. The short and long time behaviours described by (6.2) are $\sigma^2 \sim t^2$ for $t \ll \tau^\dagger$ and $\sigma^2 \sim t$ for $t \gg \tau^\dagger$, respectively.

The short time limit has been shown to explain reasonably well the early and near-field evolution of the brush for various experimental and numerical flame configurations, including spherically expanding flames and turbulent Bunsen flames (Lipatnikov & Chomiak 2002). For spatially inhomogeneous turbulent flows with a dominant direction, a convective time related to distance is used in place of time. This model suggests that the flame brush thickness scales with large, energy-containing scales of turbulence, since the ratio σ/l is a function of the normalized time $t/\tau^\dagger$ alone.

Minor adjustments to (6.1) and (6.2) are required for spherical expanding flames in decaying turbulence. Firstly, the brush thickness is defined in terms of the variance of the radial distance, so that only the radial component of the velocity vector along the Lagrangian trajectories should be considered. Since the radial direction varies along a Lagrangian trajectory, the integrand includes an orientation factor also and reads as

$$\mathrm{d}\sigma^2/\mathrm{d}t = 2u'(t)\int_0^t u'(p)f_L(p,t)\langle\cos\alpha_{p,t}\rangle\,\mathrm{d}p, \tag{6.3}$$

where the orientation factor $\langle\cos\alpha_{p,t}\rangle$ is the expectation of $\alpha_{p,t}$, the angle between two position vectors on a Lagrangian trajectory at times p and t. The derivation of (6.3) is presented in appendix B.

Since $\cos\alpha_{p,t} \leqslant 1$, (6.1) overestimates the rate of change of the brush thickness compared to (6.3). Nonetheless, the correction is small if the lateral movement on a Lagrangian trajectory during temporal intervals for which the velocity remains correlated is small compared to the radial distance of the material point. A comprehensive analysis of the orientation factor requires an investigation of Lagrangian statistics and is outside the scope of the present study. Thus, we interpret (6.1) as an upper bound on the rate of change of the brush thickness in spherically expanding flames as approximated by Taylor's theory of turbulent diffusion.

A second aspect is related to the fact that turbulence in not stationary, rather it decays in time. Batchelor & Townsend (1956) postulated that the Lagrangian velocity autocorrelation in decaying isotropic turbulence is self-similar and argued that, if the decay of the turbulent kinetic energy follows a power law (see § 3.1), there exits a characteristic time scale τ_s for which $u(t)(1+t/t_0)^{-n/2}$ is a stationary random variable in the transformed time coordinate s, defined so that $\mathrm{d}s = \mathrm{d}t/\tau_s$. Batchelor & Townsend (1956) suggested $\tau_s = t + t_0$, which was supported later by Huang & Leonard (1995) based on a model

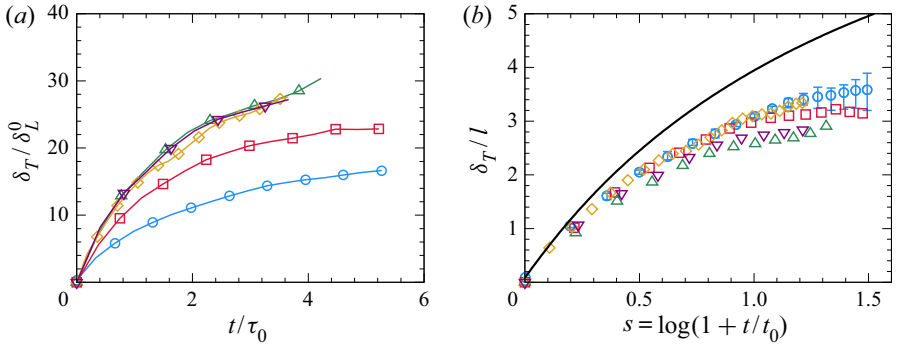

FIGURE 10. Temporal evolution of the flame brush thickness. (*a*) Brush thickness normalized by the thermal thickness of the laminar flame, δ_L^0, versus time normalized by the initial eddy turnover time. (*b*) Normalized flame brush thickness δ_T/l versus the transformed time coordinate $s = \log(1 + t/t_0)$, where $t_0 = n\tau_0$. The solid line shows the expression in (6.4), derived for the dispersion of Lagrangian particles in freely decaying isotropic turbulence with a self-similar power law decay. Symbols identify data from different simulations: *R*1 (◯), *R*2 (□), *R*2*a* (◇), *R*3 (△) and *R*3*s* (▽).

spectrum of the Lagrangian velocity autocorrelation at high Reynolds numbers. Letting $s = \log(1 + t/t_0)$ with $t_0 = n\tau_0$, all length and velocity scales in decaying turbulence are exponential functions of s. Further, as shown by Huang & Leonard (1995), the Lagrangian autocorrelation function depends on the lag between two transformed time coordinates, i.e. $f_L(t_1, t_2) = f_L(s_1 - s_2)$. The methodology for the estimation of the parameters t_0 and n was outlined in § 3.1.

Substituting the expressions for the turbulent kinetic energy (3.1) and eddy turnover time (3.2), the temporal evolution of δ_T^2 reads as

$$\delta_T^2/l^2 = (9\pi n^2)\int_0^s \mathrm{d}p \int_0^p \mathrm{d}q f_L(q-p)\exp\{(1-n/2)(p+q-2s)\}. \tag{6.4}$$

The factor in front of the integral in the above expression originates from the definition of the eddy turnover time $\tau = 3l/2u' = 3\tau^\dagger/2$ and $\tau_s = n\tau$. Equation (6.4) suggests that $\delta_T/l = f(s)$ alone and that the instantaneous integral length scale of the flow l is the obvious length to normalize the brush thickness δ_T.

Figure 10 shows the temporal evolution of the normalized flame brush δ_T/l for all simulations alongside the theoretical prediction from (6.4). The expression for the Lagrangian autocorrelation function given in Huang & Leonard (1995) was used to evaluate the integrals on the right-hand side of (6.4).

Consistent with the observations in the literature, we report good agreement of the brush thickness with the theory of turbulent diffusion early on ($s < 0.2$ or $t/\tau_0 < 0.5$) and a near collapse across simulations. This agreement is rather remarkable considering that the flame surface is defined based on the isosurface of a reactive scalar and propagates in a variable density and variable properties flow, while Taylor's theory of turbulent diffusion applies to an ensemble of material points convected by an isothermal fluid. Nonetheless, the agreement is best at early times and deviations from theory are apparent later. More importantly, the evolution of δ_T/l appears to saturate towards a limit value, while theory predicts continuous growth even in decaying turbulence.

We briefly address the deviations from the turbulent diffusion theory through the evolution equation for the brush thickness, which is derived next. The evolution equation for the flame brush thickness is readily obtained by taking the second central moment of (5.16) and reads as

$$\frac{\mathrm{d}\delta_T^2}{\mathrm{d}t} = 4\pi \int_0^\infty \langle u_r + Sn_r \rangle_w (r-R)\mathcal{P}_\phi \,\mathrm{d}r + 2\pi \int_0^\infty \langle K' \rangle_w (r-R)^2 \mathcal{P}_\phi \,\mathrm{d}r, \tag{6.5}$$

where $K' = K - K_G$ is the differential stretch rate. The first term on the right-hand side of (6.5) describes the effect of transport on the brush and consists of contributions by the mean radial velocity, velocity fluctuations and flame propagation.

We decompose the radial velocity as $u_r = \langle u_r \rangle + u_r'$, where $\langle u_r \rangle$ is the unconditional Reynolds average, so that $\langle u_r' \rangle_w$ is not zero, and the evolution equation is manipulated to read as

$$\begin{aligned}\frac{\mathrm{d}\delta_T}{\mathrm{d}t} = {} & (2\pi/\delta_T) \int_0^\infty \langle u_r' \rangle_w (r-R)\mathcal{P}_\phi \,\mathrm{d}r + (2\pi/\delta_T) \int_0^\infty \langle u_r \rangle (r-R)\mathcal{P}_\phi \,\mathrm{d}r \\ & + (2\pi/\delta_T) \int_0^\infty \langle Sn_r \rangle_w (r-R)\mathcal{P}_\phi \,\mathrm{d}r + (\pi/\delta_T) \int_0^\infty \langle K' \rangle_w (r-R)^2 \mathcal{P}_\phi \,\mathrm{d}r. \end{aligned} \tag{6.6}$$

In the order in which they appear on the right-hand side of (6.6), the terms represent contributions from velocity fluctuations or turbulent transport (term I), transport due to mean radial velocity (term II) and flame propagation (term III), and differential stretch (term IV).

Figure 11 shows $\mathrm{d}\delta_T/\mathrm{d}t$ and the four terms on the right-hand side of (6.6). All terms are normalized by the initial turbulence intensity u_0'. The rate of change of δ_T is positive for all simulations, indicating that the brush grows throughout the evolution of the turbulent flame and the behaviour and contribution of each term is similar across simulations, once normalized by the initial turbulence intensity. As time progresses, $\mathrm{d}\delta_T/\mathrm{d}t$ approaches zero, indicating that the brush thickness reaches a limit value, consistent with the temporal evolution of δ_T in figure 7(*b*).

Early in the evolution, turbulent transport (term I) dominates and contributes to the growth of the flame brush. The contribution of term I decreases in magnitude as time progresses due to the decay of turbulence and associated decrease in the fluctuation u'. Throughout the simulations, differential stretch (term IV) is negative, slowing down the rate of growth of the brush. Its magnitude grows in absolute value as time progresses. The sum of terms II (mean velocity) and III (flame propagation) is positive, but of limited importance until much later in all simulations, when u' is small.

This analysis demonstrates that the growth rate of the flame brush thickness in this configuration is controlled by the balance between two mechanisms: turbulent transport contributing to the growth of the brush and differential flame stretch impeding the growth. The turbulent flame brush approaches a constant thickness when the two contributions become equal in magnitude, but opposite in sign. We note that despite the deviations, the scaling of δ_T with l is robust, as the evolution of δ_T/l is nearly the same across different simulations. A quantitative discussion on these mechanisms and their scaling is deferred to a later work.

6.2. *Scaling of peak value of the surface density function*

Next, we address the variation of the peak value of the surface density function across simulations with varying Reynolds number. The surface density function associated with

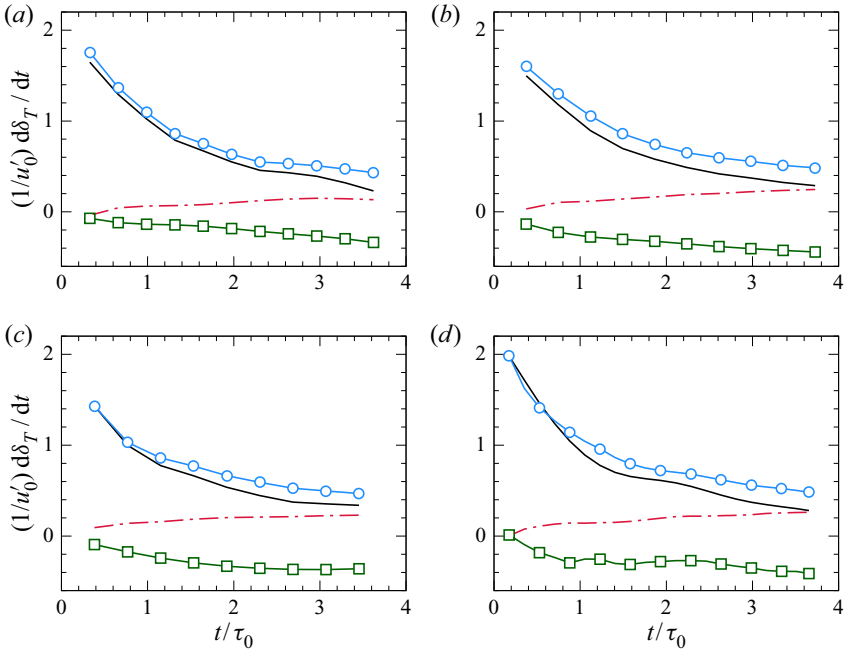

FIGURE 11. Contributions of different mechanisms in (6.6) to the growth of the flame brush thickness: $\mathrm{d}\delta_T/\mathrm{d}t$ ——, turbulent transport (term I) —◯—, mean convection and mean propagation (sum of terms II and III) — · —, and differential stretch (term IV) —□—. All terms are normalized by the initial turbulence intensity u_0'. Data shown for (*a*) *R*1, (*b*) *R*2, (*c*) *R*3 and (*d*) *R*2*a*.

the isosurface $C = c$ (Vervisch *et al.* 1995) reads as

$$\Sigma(r, t; c) = \langle |\nabla C| | C = c \rangle \mathcal{P}_C(c; r, t), \tag{6.7}$$

where $\mathcal{P}_C$ is the PDF of the progress variable C and angular brackets denote ensemble averaging.

Figure 12(*a*) shows $\langle |\nabla C| | C = c \rangle$ as a function of c at early times ($t/\tau_0 = 0.75$) and towards the end ($t/\tau_0 = 5.25$) of simulation *R*2. The conditional mean of the gradient is very close to that found across the one-dimensional laminar flame, confirming that the turbulent flames belong to the thin flamelet regime (Peters 2000). Furthermore, at each instant, the gradient is normalized by δ_L^0 in order to highlight that the effect of pressure on the flame structure is minor as the peak value of the gradient changes by 10 % only. Figure 12(*b*) shows the radial variation of $\langle |\nabla C| | C = c^* \rangle$ across the brush at $t/\tau_0 = 5.25$, indicating that the conditional gradient magnitude grows only very slightly across the brush and may be considered constant for all practical purposes.

Thus, we conclude that the conditional gradient magnitude $\langle |\nabla C| | C = c^* \rangle$ is independent of radial location r and time t also, so that any spatial and temporal dependence of the surface density function Σ is due to $\mathcal{P}_C(c^*; r, t)$.

In order to investigate the scaling and spatial dependence of $\mathcal{P}_C$, we consider an ensemble of two-dimensional plane cuts, whereby each plane contains the origin and its normal is oriented randomly. On each plane cut, we consider a circle of radius r, centred at the origin, and let $\boldsymbol{e}_t$ be the unit vector along the tangential direction. Let q be the arc length distance from an arbitrary point along the circle ($0 \leqslant q < 2\pi r$). Figure 13(*a*) shows

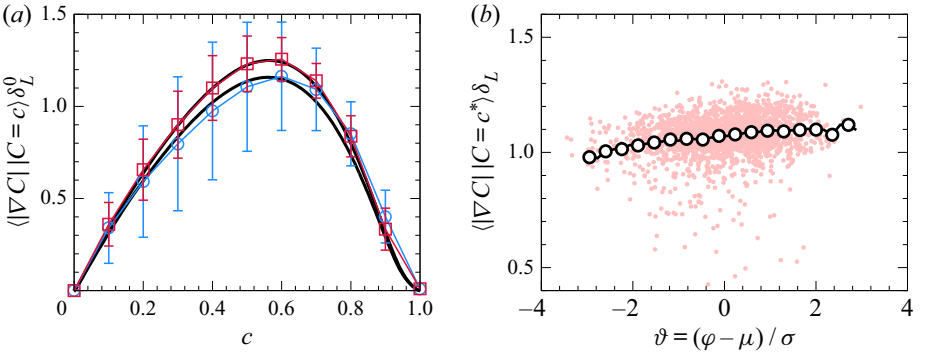

FIGURE 12. Conditional statistics of the gradient magnitude. Data from simulation *R*2. (*a*) Conditional mean gradient magnitude from DNS (blue and red lines), one-dimensional laminar flame (black lines) at two different times, normalized by the thermal thickness of the laminar flame δ_L^0. Data shown at $t/\tau_0 = 0.75$ (blue line with open circles) and $t/\tau_0 = 5.25$ (red line with open squares). The error bars represent the conditional standard deviation. (*b*) Radial distribution of the conditional mean gradient magnitude ($C = c^*$) at $t/\tau_0 = 5.25$. Scatter of samples is represented with small solid circles. Gradients are multiplied by the laminar flame thermal thickness $\delta_L(t)$.

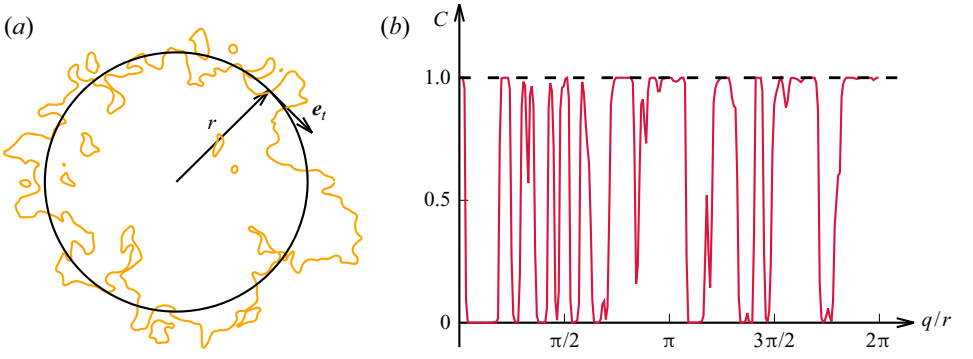

FIGURE 13. Flame surface crossings in a plane for simulation *R*2 at $t/\tau_0 = 4.5$. (*a*) Cut of the flame surface $C = c^*$. (*b*) Progress variable field along a circle of radius r versus the normalized arc length q/r.

a schematic representation of one such planar cut. The progress variable C as a function of the coordinate q along one such circle is shown in figure 13(*b*).

Given the spherical symmetry of the statistics, the progress variable C and its gradient ∇C are ergodic along $\boldsymbol{e}_t$. The probability $\mathbb{P}$ that C takes a value between $c - \mathrm{d}c/2$ and $c + \mathrm{d}c/2$ on the circle is

$$\mathbb{P}[c - \mathrm{d}c/2 \leqslant C \leqslant c + \mathrm{d}c/2] = \mathcal{P}_C(c; r, t)\,\mathrm{d}c = \frac{1}{p2\pi r}\sum_{j=1}^{p}\sum_{i=1}^{m_j}\mathrm{d}q_{ij}, \tag{6.8}$$

where $\mathrm{d}q_{ij}$ is an infinitesimal arc length centred at location q_{ij} such that $C(q_{ij}) = c$ and $c - \mathrm{d}c/2 \leqslant C(q) \leqslant c + \mathrm{d}c/2$ for $q_{ij} - \mathrm{d}q_{ij}/2 \leqslant q \leqslant q_{ij} + \mathrm{d}q_{ij}/2$ and m_j is the number of locations along circle j ($j = 1, \ldots, p$). Similar to the nomenclature used in the

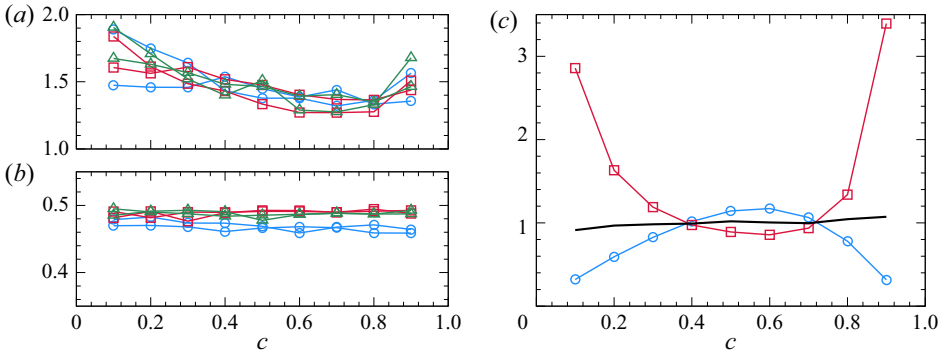

FIGURE 14. (*a*) The Υ factor and (*b*) alignment $\langle|\cos\alpha_{nt}||C=c\rangle$ statistics for three simulations at two select times: $R1$ (◯), $R2$ (□) and $R3$ (△). (*c*) Peak surface density function Σ_m (thick line), PDF of progress variable $\mathcal{P}_C$ (□), and conditional mean of the gradient magnitude $\langle|\nabla C||C=c\rangle$ (◯) at $r=R(t)$, normalized by their corresponding values for $c=c^*$. Data from simulation $R2$.

Bray–Moss–Libby (BML) model (Bray & Moss 1977; Libby & Bray 1980), each of the q_{ij} locations is referred to as a flame crossing.

Each infinitesimal arc length $\mathrm{d}q_{ij}$ is related to the projection of the gradient ∇C onto the tangential vector $\boldsymbol{e}_t$ at the flame crossing i with circle of radius r on plane j:

$$\mathrm{d}q_{ij} = \mathrm{d}c/|\nabla C\cdot\boldsymbol{e}_t|_{ij}. \tag{6.9}$$

Let m indicate the total number of flame crossings summed over all planes. Rearranging (6.8) and dividing by $\mathrm{d}c$, we have

$$\mathcal{P}_C(c;r,t) = \frac{m}{p2\pi r}\frac{1}{m}\sum_{j=1}^{p}\sum_{i=1}^{m_j}|\nabla C\cdot\boldsymbol{e}_t|_{ij}^{-1} \tag{6.10}$$

$$= \varpi(r,t)\,\langle|\nabla C\cdot\boldsymbol{e}_t|^{-1}|C=c\rangle, \tag{6.11}$$

where $\varpi(r,t)=m/(p2\pi r)$ is the flame crossing frequency, defined as the number of flame crossings per unit length. The average of $|\nabla C\cdot\boldsymbol{e}_t|^{-1}$ over all crossings on circles of radius r is simply the conditional average of $|\nabla C\cdot\boldsymbol{e}_t|^{-1}$ at the radial location r.

Since the expression for Σ involves the conditional mean of $|\nabla C|$, it is beneficial to relate the conditional mean of the inverse $|\nabla C\cdot\boldsymbol{e}_t|^{-1}$ to the inverse of the conditional mean directly as

$$\langle|\nabla C\cdot\boldsymbol{e}_t|^{-1}|C=c\rangle = \Upsilon\,\langle|\nabla C\cdot\boldsymbol{e}_t||C=c\rangle^{-1}, \tag{6.12}$$

where Υ is given by

$$\Upsilon = 1 + Var\left\{|\nabla C\cdot\boldsymbol{e}_t||C=c\right\}/\langle|\nabla C\cdot\boldsymbol{e}_t||C=c\rangle^2 + \ldots. \tag{6.13}$$

We find that $\Upsilon\approx 1.35$ for $0.5\leqslant c\leqslant 0.9$ across all simulations at all times as shown in figure 14(*a*). In the limit of infinitesimally thin turbulent premixed flames, $\Upsilon\to 1$.

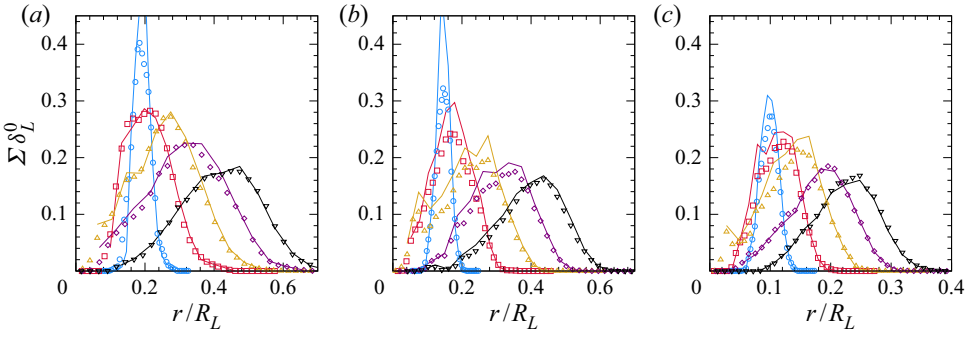

FIGURE 15. Comparison between the two expressions for Σ in (6.16) and the direct evaluation from the gradients for three simulations at five times: (*a*) *R*1, (*b*) *R*2 and (*c*) *R*3. Time increases from left to right.

Assuming that the projection of the flame normal $\boldsymbol{n}$ onto $\boldsymbol{e}_t$ and the gradient magnitude are uncorrelated, we write

$$\langle |\nabla C|\, |\boldsymbol{n}\cdot\boldsymbol{e}_t||C=c\rangle \approx \langle |\nabla C||C=c\rangle\langle |\boldsymbol{n}\cdot\boldsymbol{e}_t||C=c\rangle. \tag{6.14}$$

The assumption that the two are uncorrelated appears to be reasonable on the account that turbulence in the reactants is isotropic. Then, $\mathcal{P}_C$ reads as

$$\mathcal{P}_C(c;r,t) = \frac{\varpi(r,t)\Upsilon}{\langle |\nabla C||C=c\rangle\langle |\cos\alpha_{nt}||C=c\rangle}, \tag{6.15}$$

where $|\boldsymbol{n}\cdot\boldsymbol{e}_t| = |\cos\alpha_{nt}|$ and α_{nt} is the angle between the normal $\boldsymbol{n}$ and the ergodic direction $\boldsymbol{e}_t$ and represents the orientation of the flamelets with respect to the ergodic direction. We find that the orientation angle α_{nt} is nearly constant in time, independent of the conditioning value c, and the same across simulations. As a result, Σ is independent of the conditioning value c for $0.1 \leqslant c \leqslant 0.9$ as shown in figure 14(*c*), since $\mathcal{P}_C \sim 1/\langle |\nabla C||C=c\rangle$.

Based on the above analysis, an approximate expression for the surface density function is

$$\Sigma(r,t;c) = \varpi(r,t)\Upsilon/\langle |\cos\alpha_{nt}||C=c\rangle. \tag{6.16}$$

Figure 15 compares the left- and right-hand sides of (6.16) for $c = 0.73$, which are found to be in good agreement. Since the factor $\Upsilon/\langle |\cos\alpha_{nt}||C=c\rangle$ is approximately constant in space, time and across simulations, the spatial and temporal dependence of $\Sigma = \Sigma(r,t)$ is solely due to that of the crossing frequency $\varpi = \varpi(r,t)$.

This result is consistent with the Bray–Moss–Libby theory of turbulent premixed combustion, whereby the surface density function is modelled in terms of the spatial crossing frequency and a mean cosine factor as $\Sigma = \varpi/\langle |\cos\alpha_{nt}|\rangle$ (Bray, Libby & Moss 1984; Bray & Libby 1986). Here we find a similar expression with the additional factor $\Upsilon = O(1)$, which provides a correction for the fact that premixed flames are not infinitesimally thin and Υ is not strictly unity.

For a statistically stationary and planar turbulent premixed flame, the BML model relates the crossing frequency ϖ to the two-point, one-time autocorrelation function of

the progress variable

$$\mathcal{F}(q; x_1) = \langle C'(\boldsymbol{x}, t)C'(\boldsymbol{x} + q\boldsymbol{e}_\alpha, t)\rangle/\sigma_C^2, \tag{6.17}$$

$$\varpi = \varpi(x_1) = -2\partial\mathcal{F}/\partial q|_{q=0}, \tag{6.18}$$

where x_1 is the inhomogeneous coordinate normal to the plane of the flame, $C' = C - \langle C\rangle$ is the fluctuation field, $\sigma_C^2 = \langle(C - \langle C\rangle)^2\rangle$ is the variance and $\boldsymbol{e}_\alpha$ is a unit vector in the plane of the flame that identifies an ergodic direction. Under specific assumptions on the functional form of the autocorrelation function $\mathcal{F}$, the crossing frequency and surface density function read as

$$\varpi = A_\varpi\langle C\rangle(1 - \langle C\rangle)/L^*, \tag{6.19}$$

$$\Sigma = A_\Sigma\langle C\rangle(1 - \langle C\rangle)/L^*, \tag{6.20}$$

where $\langle C\rangle = \langle C\rangle(x_1)$, A_ϖ and A_Σ are constants of order unity, and L^* is the so-called wrinkling scale.

Since the crossing frequency is closely related to the autocorrelation function of the progress variable (Bray *et al.* 1984; Bray & Libby 1986), L^* likely reflects the entire spectrum of the progress variable turbulent field $C(\boldsymbol{x}, t)$, although it is not clear how L^* should scale with the Reynolds number and how a suitable autocorrelation length could be defined from the autocorrelation function.

There exists significant controversy on the origin and values taken by the wrinkling scale in the literature. Cant & Bray (1989) proposed the following closure for the wrinkling scale,

$$L^* \propto k^{3/2}\epsilon^{-1}, \tag{6.21}$$

thereby advancing the hypothesis that the wrinkling scale is proportional to the integral scale defined as $l = u'^3/\epsilon$ and controlled by turbulence and energy-containing fluid motions, rather than flame propagation. Deschamps *et al.* (1992) observed $L^* \approx l$ for conical turbulent premixed flames, while others (Veynante, Duclos & Piana 1994; Shy *et al.* 2000) found that the wrinkling scale is about five times smaller than the integral scale for V-shaped and planar turbulent premixed flames. Further, Shy *et al.* (2000) reported that the wrinkling scale remained constant for two different turbulence intensities, while the integral length scale changed by ≈50 %. However, inadequate resolution of the turbulent flame surface may be responsible for this observation, as the wrinkling scale was found to be of the size as the width of the averaging box used for the measurement of the surface density function. Finally, dependence of L^* on u'/S_L has been postulated also, yet no conclusive evidence exists.

Given that L^* and $1/\Sigma$ are related to within constants of order unity, we define the wrinkling scale as $L^* = (4\Sigma_m)^{-1}$, where Σ_m is the peak surface density in (5.19). The factor of 4 is included so as to be consistent with (6.20), since the peak surface density Σ_m occurs near $\langle C\rangle = 0.5$. The proportionality $L^* \propto 1/\Sigma_m$ highlights that both quantities obey the same scaling laws.

Figure 16(*a*) shows the temporal evolution of Σ_m normalized by the thermal thickness of the laminar premixed flame. It is apparent that Σ_m decreases in time several fold for each simulation. Because δ_L^0 is constant across simulations and the variation in the flame thickness is minimal during the propagation of the turbulent flames, figure 16(*a*) shows conclusively that Σ_m does not scale with the thermal thickness of the laminar flame. This behaviour is consistent with experiments on turbulent spherical flames in decaying turbulence behind grids (Renou *et al.* 2002; Fries *et al.* 2019).

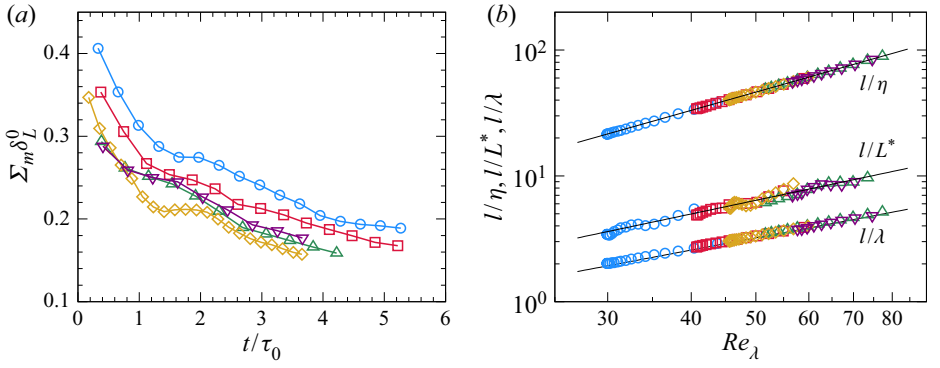

FIGURE 16. (*a*) Peak flame surface density Σ_m normalized by the thermal flame thickness δ_L^0. (*b*) Ratio of length scales and power law fits aRe_λ^b (solid lines). We observe $l/\eta \sim Re_\lambda^{1.5}$, $l/\lambda \sim Re_\lambda^{1.0}$ and $l/L^* \sim Re_\lambda^{1.13}$. Thus, L^* lies between η and λ with separation increasing with Re_λ. Symbols in both (*a*,*b*) represent data from various simulations: *R*1 (◯), *R*2 (□), *R*2*a* (◇), *R*3 (△) and *R*3*s* (▽).

Figure 16(*b*) shows L^* normalized by the integral scale l and plotted against Re_λ. Data from all flame configurations and several times during each simulation are shown. It is apparent that over the range $30 \leqslant Re_\lambda \leqslant 85$, L^* is about 5 to 10 times smaller than the integral length scale. Further, the wrinkling scale falls between the Taylor scale λ and Kolmogorov scale η, albeit closer to the former than to the latter. When scaled with l, the data suggest the following power law fit for the wrinkling scale:

$$l/L^* = 4\Sigma_m l = 0.0756 Re_\lambda^{1.13}. \tag{6.22}$$

Note that only data for $t/\tau_0 > 0.5$ have been used in the fit since it is necessary for turbulent motions to wrinkle the flame past an initial transient, during which a power law scaling for l/L^* is not warranted.

The power law scaling from (6.22) shown in figure 16(*b*) is rather convincing, especially because it holds across simulations and instantaneously even as Re_λ and l vary in time during the decay of turbulence. Nonetheless, studies over a broader range of Reynolds number are obviously desirable.

The observation that $\eta < L^* < \lambda$ suggests that the peak surface density is governed by small scales. The importance of small scales in controlling Σ_m has been postulated by Huh, Kwon & Lee (2013), who analysed the surface density transport equation for statistically planar flames and proposed that Σ_m scales with the inverse of the mean flame surface curvature. Since Zheng, You & Yang (2017) demonstrated that the PDF of the flame surface curvature is independent of the Reynolds number when normalized with the Kolmogorov length, a case could be made that $\Sigma_m \propto \eta^{-1}$, independently of Re_λ. Our data do not support this conclusion, although they do highlight the fact that L^* is smaller than λ and its evolution is most likely related to processes at the dissipative end of the inertial range of the turbulence spectrum.

The Darrieus–Landau (DL) instability (Darrieus 1938; Landau 1944) may provide an additional mechanism for flame surface wrinkling (Fogla, Creta & Matalon 2013; Creta *et al.* 2016), thereby influencing the surface density distribution and the wrinkling scale. The instability may be particularly important towards the end of the simulations, as pressure and flame radius increase, while turbulence decays leading to small u'/S_L.

The importance of the DL instability in the present flames may be assessed by comparing the growth rates of the DL instability against the rates of flame wrinkling in the range of wavenumbers where both effects are active. It is assumed that the range of scales over which the DL instability is important is $\kappa \in [1/R, 1/\delta_L]$, while that of turbulent wrinkling is $\kappa \in [1/l, 1/\eta]$. Since $R > l$ and $\eta < \delta_L$ at all times, the overlap region is $\kappa \in [1/l, 1/\delta_L]$. Following the analysis in Yang *et al.* (2018), the ratio is

$$\omega_T(\kappa)/\omega_{DL}(\kappa) \approx u'_\kappa/S_L, \tag{6.23}$$

where $u'_\kappa = (\epsilon/\kappa)^{1/3}$ is the eddy velocity associated with wavenumber κ. Since $u'_\kappa/S_L > u'_\eta/S_L > 1$ for all κ in the overlap region, we conclude that all turbulent flames considered in this study belong to the turbulence dominated regime (Yang *et al.* 2018), and the effect of DL instability can be safely neglected.

6.3. *Scaling of the area ratio*

The findings in §§ 6.1 and 6.2 have critical implications with regard to the evolution of the area ratio χ and its values across flame configurations. We begin by rearranging (5.20*a*) into

$$\chi = \Sigma_m \delta_T \beta = (l/4L^*)(\delta_T/l)\beta. \tag{6.24}$$

Recalling that β is a shape factor that is nearly constant and substituting the scaling laws for the brush and peak surface density function, we obtain

$$\chi(t) = C_\chi Re_\lambda^{1.13} f(s), \tag{6.25}$$

where C_χ is a constant and the dependence of δ_T/l on time is captured by $f(s)$ with $s = \log(1 + t/t_0)$ indicating the transformed time coordinate. The area ratio χ and $S_T/S_L \sim \chi$ depend on time directly due to $\delta_T/l \sim f(s)$ and indirectly due to $Re_\lambda = Re_\lambda(t)$ in decaying turbulence.

The most important implication of (6.25) is that

$$\chi(t) Re_\lambda^{-1.13} \sim f(s), \tag{6.26}$$

so that if two turbulent spherical flames are compared at the same logarithmic time s, the area ratio χ scales as $Re_\lambda^{1.13}$ or as $Re^{0.56}$, since $Re = u'l/\nu \sim Re_\lambda^2$. This observation is broadly consistent with the previously reported Reynolds dependence of burning rates in spherical turbulent flames (Chaudhuri *et al.* 2012; Jiang *et al.* 2016; Ahmed & Swaminathan 2013).

Figure 17(*a*) shows that χ varies in time and across flame configurations. For $t/\tau_0 > 2$, χ reaches a limit value, which differ for each case by as much as a factor of 1.6. The same data are shown in compensated form as $\chi(t) Re_\lambda^{-1.13}$ versus s in figure 17(*b*). Note that only data for $t/\tau_0 > 0.5$, which corresponds to $s > 0.3$, are shown because the scaling of Σ_m implies that turbulent motions have had sufficient time to wrinkle the flame past an initial transient, during which the power law scaling l/L^* in (6.22) is not applicable.

The collapse in figure 17(*b*) is encouraging, albeit not perfect, especially for the data from simulations *R*3 and *R*3*s* at later times $s > 1$. Despite minor inconsistencies, which are related to the imperfect collapse of δ_T/l at later times as shown in figure 10(*b*), we conclude that scale separation, as parametrized by the Reynolds number plays an important role in controlling the area ratio and the dimensionless turbulent flame speed $S_T/S_L \sim \chi$ across flame configurations.

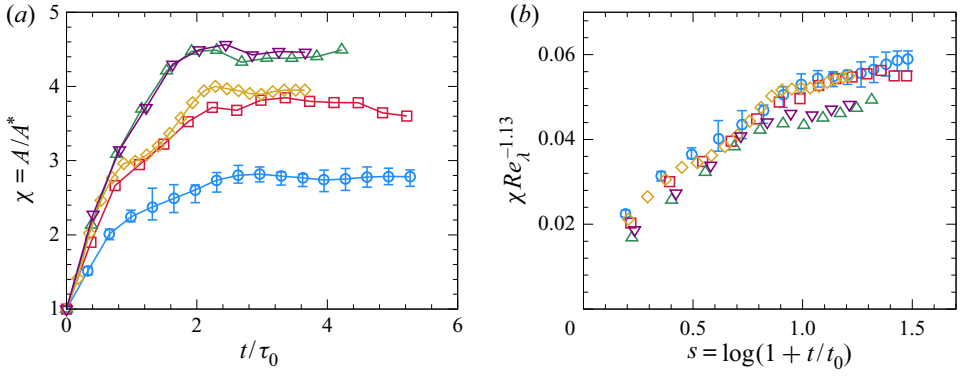

FIGURE 17. (*a*) Area ratio versus time t/τ_0. (*b*) Area ratio compensated with the proposed Reynolds scaling versus the transformed time coordinate $s = \log(1 + t/t_0)$ with $t_0 = n\tau_0$. Symbols represent data from simulations: *R*1 (◯), *R*2 (□), *R*2*a* (◇), *R*3 (△) and *R*3*s* (▽).

In order to investigate this important implication, three simulations are considered. These include *R*2 and *R*2*a*, which share the same Reynolds number, but not the same u'/S_L, and simulations *R*1 and *R*2*a*, which share u'/S_L, but not the same Reynolds number. Note that u'/S_L changes in time as reported in figure 3(*c*).

From the evolution of χ for *R*1, *R*2 and *R*2*a* in figure 17(*a*), it is clear that when the Reynolds number is held constant and u'/S_L changes (along with l/δ_L), the area ratio does not change (*R*2 vs. *R*2*a*). On the other hand, when u'/S_L is held constant and the Reynolds number changes (along with l/δ_L), the area ratio is greater for the flame with the higher Reynolds number (*R*1 vs. *R*2*a*). These results support the conclusion that, for a given premixed mixture, S_T/S_L is not a function of u'/S_L at constant Reynolds number for the flame configuration and regime considered. A similar Reynolds dependence was proposed by Chaudhuri *et al.* (2011) based on spectral analysis of the level-set equations. Because when u'/S_L is held constant as Re_λ increases, the ratio l/δ_L increases proportionally also (for the same reactive mixture, pressure and temperature), the observed trends in χ may not be conclusively attributed solely to Re_λ independently of l/δ_L and a broader set of simulations are required.

In closing, we remark that in most experiments on turbulent premixed flames, the integral scale of the flow remains approximately constant as u' is varied by increasing flow rates or fan speeds. This occurrence is due to the fact that the integral scales are largely set by the geometrical details of the burner, turbulence-generating grids, or fans, which are held fixed for practical reasons. The consequence is that both u'/S_L and Re vary together at $l/\delta_L \approx const$ in most studies. Then, with l/δ_L constant as u'/S_L increases holding premixed reactants, kinematic viscosity (i.e. pressure), and burner geometry unchanged, one obtains $S_T/S_L \sim (u'/S_L)^{0.55}$ since $S_T/S_L \sim Re^{0.55}$.

7. Summary and conclusions

The propagation of spherical turbulent premixed methane/air flames in decaying turbulence was investigated at different conditions via direct numerical simulations. The simulations feature detailed finite rate chemistry for methane oxidation and mixture-average transport. The simulations are repeated for several values of the Taylor-scale Reynolds number Re_λ, where all properties of isotropic turbulence are defined

in the reactants. By design, the extent of the turbulent flame is large compared to the integral length scale of turbulence, guaranteeing that the flame surface is wrinkled by motions across the entire spectrum of turbulence and that statistics are duly converged. The flames belong to the thin reaction zone regime of turbulent premixed combustion and are characterized by low values of the Karlovitz number, so that the dimensionless turbulent flame speed is equal to the area ratio, defined as the ratio of the area of the flame surface to a reference area based on the mean progress variable. Thus, enhancements to the burning rate are brought by flame wrinkling, folding and stretching.

The data are analysed within the formalism of the surface density function and under the assumption of spherical symmetry of the statistics. The analysis shows that the dimensionless turbulent flame speed is equal to the product of the flame brush thickness, the peak value of the surface density function and a non-dimensional shape factor of order unity. This decomposition lies at the basis of our postulate that the area ratio of turbulent premixed flames increases for increasing scale separation.

Once scaled by the instantaneous value of the integral length scale and plotted versus a stretched logarithmic time coordinate consistent with the evolution of turbulent kinetic energy in decaying homogeneous isotropic turbulence, the flame brush thickness is found to be nearly self-similar across simulations, irrespective of the Reynolds number of the flow. This result is significant because it indicates that the extent of the turbulent flame brush is governed by the largest scales of the flow as suggested by past experiments.

An ordinary differential equation that describes the evolution of the brush thickness is derived and indicates that the growth of the brush is controlled primarily by the balance of two mechanisms. Turbulent diffusion by velocity fluctuations leads to an increase in the brush thickness, consistent with Taylor's theory of turbulent diffusion, while spatial variations of the statistics of flame stretch across the brush lead to a decrease in its thickness. Early in the evolution, the brush grows rapidly due to turbulent transport, but later the two contributions balance each other and the brush thickness appears to reach an asymptotic limit.

Following the framework of the Bray–Moss–Libby model of turbulent premixed combustion, we relate the peak value of the surface density function to the flamelet spatial crossing frequency, so that its inverse is the wrinkling length scale. The concept of wrinkling length is noteworthy because it allows us to scale the surface density function across simulations. For all cases, we find that the wrinkling length is larger than the Kolmogorov scale, but smaller than the Taylor micro-scale, being closer to the latter than to the former. Most important, the ratio between the wrinkling scale and the integral scale of the flow is proportional to $Re_\lambda^{-1.13}$ across all simulations. This result identifies the wrinkling scale as a hydrodynamic scale related to turbulence and its spectrum.

The evolution and scaling of the brush and peak surface density function result in the dimensionless turbulent flame speed scaling as $S_T/S_L Re_\lambda^{-1.13} \sim f(s)$, where s is the suitable logarithmic time coordinate for decaying turbulence and $f(s)$ is a function that describes the growth of the brush normalized by the integral scale. The scaling is shown to hold to a very good approximation over several cases with $30 \leqslant Re_\lambda \leqslant 80$.

At present, the origin of the value of the scaling exponent is unclear and it is possible that it is somewhat specific to the spherical flame configuration. Furthermore, the results shown pertain to a modest range of Reynolds numbers and little separation exists between the dissipative scales and the wrinkling scale. More definitive conclusions require higher values of the Reynolds number. Finally, the flame configurations feature low values of the Karlovitz number, so that it is unclear whether the ratio of the Kolmogorov time to the flame time scale plays an additional role in the scaling.

Despite the limitations in scope, our data support the notion that scale separation, as parametrized by the Reynolds number, is a key parameter in controlling the burning rates of the spherical turbulent premixed flames at the conditions explored in the simulations. Broadly, the fact that $S_T/S_L \sim Re_\lambda^{1.13}$ points to the key role of the integral length scale l and kinematic viscosity ν, in addition to that of the velocity fluctuation u', which is well recognized in the literature. Our analysis provides a novel perspective that is consistent quantitatively with recent experimental results.

Acknowledgements

This material is based upon work supported in part by the National Science Foundation (NSF) under grant number 1805921. Numerical simulations were carried out on the 'Shaheen' supercomputer at King Abdullah University of Science and Technology (KAUST) and on the 'Stampede 2' supercomputer at the Texas Advanced Computing Center (TACC) through allocation TG-CTS180002 under the Extreme Science and Engineering Discovery Environment (XSEDE). XSEDE is supported by the NSF under grant number ACI-1548562. Any opinions, findings and conclusions or recommendations expressed in this material are those of the authors and do not necessarily reflect the views of the NSF.

Declaration of interests

The authors report no conflict of interest.

Supplementary movies

Supplementary movies are available at https://doi.org/10.1017/jfm.2020.784.

Appendix A. Estimation of $R(t)$ and $A(t)$

Define the flame surface area as a random process $\tilde{A}(t)$ with $\tilde{A}^{(n)}(t)$ denoting its repetition n of $\mathcal{N}$. Then, the mean of the flame surface area is

$$A(t) \equiv \langle \tilde{A}(t) \rangle = \langle \langle \tilde{A}(t) \rangle_{\mathcal{N}} \rangle = \left\langle \frac{1}{\mathcal{N}} \sum_{n=1}^{\mathcal{N}} \tilde{A}^{(n)}(t) \right\rangle, \tag{A 1}$$

where $\langle \cdot \rangle$ denotes statistical expectation and $\langle \cdot \rangle_{\mathcal{N}}$ indicates ensemble averaging over $\mathcal{N}$ repetitions (Pope 2000).

The random process $\tilde{A}(t)$ is functionally related to the progress variable random field $C(\boldsymbol{x}, t)$ (Maz'ya 1985),

$$\tilde{A}(t) = \int_V |\nabla C(\boldsymbol{x}, t)| \delta[C(\boldsymbol{x}, t) - c^*] \, \mathrm{d}V, \tag{A 2}$$

where δ is the Dirac delta function and $C(\boldsymbol{x}, t) = c^*$ is the isosurface taken to represent the flame, so that

$$A(t) \equiv \langle \langle \tilde{A}(t) \rangle_{\mathcal{N}} \rangle = \left\langle \left\langle \int_V |\nabla C| \delta(C - c^*) \, \mathrm{d}V \right\rangle_{\mathcal{N}} \right\rangle. \tag{A 3}$$

Rearranging the order by which the statistical expectation, ensemble average and volumetric integral are taken, we obtain

$$A(t) = \int_V \langle\langle |\nabla C|\delta(C - c^*)\rangle\rangle_{\mathcal{N}}\, \mathrm{d}V = \int_V \langle\langle \tilde{\Sigma}\rangle\rangle_{\mathcal{N}}\, \mathrm{d}V, \tag{A 4}$$

where we defined the spherically symmetric random field $\tilde{\Sigma}(\boldsymbol{x}, t) = |\nabla C|\delta(C - c^*)$ with expectation $\langle\tilde{\Sigma}\rangle$. For each repetition n of $\mathcal{N}$, spherical averaging of $\tilde{\Sigma}$,

$$\langle\tilde{\Sigma}\rangle_{\Theta\Phi} = \frac{1}{4\pi r^2}\int_0^{2\pi}\int_0^{\pi} \tilde{\Sigma}(r, \Theta, \Phi, t) r^2 \sin\Theta\, \mathrm{d}\Theta\, \mathrm{d}\Phi, \tag{A 5}$$

is an estimate for $\langle\tilde{\Sigma}\rangle$ consistent with the statistical symmetry of the random field. Based on (A 5), we rewrite (A 4) as

$$A(t) \equiv \langle\tilde{A}(t)\rangle \approx \int_V \langle\langle\tilde{\Sigma}\rangle_{\Theta\Phi}\rangle_{\mathcal{N}}\, \mathrm{d}V = 4\pi\int_0^{\infty} r^2\langle\langle\tilde{\Sigma}\rangle_{\Theta\Phi}\rangle_{\mathcal{N}}\, \mathrm{d}r. \tag{A 6}$$

In the last step, we exploited the fact that $\langle\tilde{\Sigma}\rangle_{\Theta\Phi}$ depends on (r, t) only.

The mean of the flame surface area is the volumetric integral of the flame surface density function Σ (Pope 1988; Vervisch *et al.* 1995),

$$A(t) = \int_V \Sigma\, \mathrm{d}V = 4\pi\int_0^{\infty} r^2\Sigma(r, t)\, \mathrm{d}r, \tag{A 7}$$

with Σ a function of (r, t) only in the present unsteady spherically symmetric configuration. Equating (A 7) and (A 6) brings

$$A(t) = 4\pi\int_0^{\infty} r^2\Sigma\, \mathrm{d}r \approx 4\pi\int_0^{\infty} r^2\langle\langle\tilde{\Sigma}\rangle_{\Theta\Phi}\rangle_{\mathcal{N}}\, \mathrm{d}r, \tag{A 8}$$

which implies, as expected, that $\langle\langle\tilde{\Sigma}\rangle_{\Theta\Phi}\rangle_{\mathcal{N}}$ is an approximation to Σ and that the statistical error inherent in the estimate of $A(t)$ depends on the number of repetitions $\mathcal{N}$ and the variance of the spherical average $\langle\tilde{\Sigma}\rangle_{\Theta\Phi}$.

The central limit theorem may be applied to spherical averages of spatially discrete solutions noting that surface averages are approximated by summations so that $Var[\langle\tilde{\Sigma}\rangle_{\Theta\Phi}] = Var[\tilde{\Sigma}]/\mathcal{M}_r$, where $Var[U]$ indicates the variance of a random variable U and $\mathcal{M}_r$ is the number of independent and identically distributed (i.i.d.) samples gathered on the surface of radius r.

The present configurations were designed to have large R/l ratios, i.e. the flame radius is large compared to the integral scale of velocity, leading to very many i.i.d. samples of $\tilde{\Sigma}$. Consequently, $Var[\langle\tilde{\Sigma}\rangle_{\Theta\Phi}]$ is small and one repetition ($\mathcal{N} = 1$) is sufficient to obtain a close estimate of the mean of both the flame surface density function and flame surface area at time t.

Similar considerations apply to $R(t) = \langle \tilde{R}(t) \rangle$ by defining the random process (Maz'ya 1985)

$$\tilde{R}(t) = \frac{1}{A(t)} \int_V r(\boldsymbol{x}) |\nabla C(\boldsymbol{x}, t)| \delta[C(\boldsymbol{x}, t) - c^*] \, \mathrm{d}V, \tag{A 9}$$

which is the instantaneous surface averaged Euclidean (radial) distance $r(\boldsymbol{x}) = |\boldsymbol{x}|$ of the flame surface from the origin located at the centre of the computational domain. Then

$$R(t) \equiv \langle \tilde{R}(t) \rangle = \langle \langle \tilde{R}(t) \rangle_{\mathcal{N}} \rangle \approx \frac{4\pi}{A(t)} \int_0^\infty r^3 \langle \langle \tilde{\Sigma} \rangle_{\Theta\Phi} \rangle_{\mathcal{N}} \, \mathrm{d}r. \tag{A 10}$$

Appendix B. Dispersion relation in spherical coordinate system

Taylor's theory of turbulent diffusion (Taylor 1922) describes the dispersion of material points in homogeneous isotropic turbulence. Its application to dispersion in radial coordinates requires modifications to account for changes in the radial direction along Lagrangian trajectories. Consider an ensemble of particles released on a sphere of radius R_0 at time $t = 0$ in decaying homogeneous isotropic turbulence. The radial distance $r(a, t)$ of a particle with index a at $t > 0$ is given by

$$r(a, t) = |\boldsymbol{x}(a, t)|, \tag{B 1}$$

where $\boldsymbol{x}$ is the position vector of the particle with respect to the origin.

The evolution of the particle's radial distance is governed by

$$\frac{\mathrm{d}r(a, t)}{\mathrm{d}t} = \boldsymbol{u}(\boldsymbol{x}(a, t), t) \cdot \boldsymbol{i}_r(a, t), \tag{B 2}$$

where $\boldsymbol{u}$ denotes the local fluid velocity vector at the particle location and $\boldsymbol{i}_r$ is the unit vector in radial direction $\boldsymbol{i}_r(a, t) = \boldsymbol{x}(a, t)/|\boldsymbol{x}(a, t)|$. Integrating the ordinary differential equation with initial condition $r(a, 0) = R_0$ gives the particle's distance for $t > 0$,

$$r(a, t) = R_0 + \int_0^t \boldsymbol{u}(\boldsymbol{x}(a, p), p) \cdot \boldsymbol{i}_r(a, p) \, \mathrm{d}p. \tag{B 3}$$

Here p represents the dummy variable of integration.

Following Taylor (1922), the variance σ^2 of the radial distance in the absence of mean radial velocity is

$$\frac{1}{2} \frac{\mathrm{d}\sigma^2}{\mathrm{d}t} = \left\langle (r(a, t) - R_0) \frac{\mathrm{d}r}{\mathrm{d}t}(a, t) \right\rangle = \left\langle \boldsymbol{u}(a, t) \cdot \boldsymbol{i}_r(a, t) \int_0^t \boldsymbol{u}(a, p) \cdot \boldsymbol{i}_r(a, p) \, \mathrm{d}p \right\rangle, \tag{B 4}$$

since the mean radial distance is constant and equal to R_0. In the above expression, angular brackets denote average over the ensemble of particles and the dependence of $\boldsymbol{u}$ on $\boldsymbol{x}(a, p)$ is written as $\boldsymbol{u}(a, p)$.

The above integral reads as

$$\frac{1}{2}\frac{\mathrm{d}\sigma^2}{\mathrm{d}t} = \int_0^t \left\langle u_x(a,t)u_x(a,p)\frac{x(a,t)x(a,p)}{r(a,t)r(a,p)}\right\rangle \mathrm{d}p + \int_0^t \left\langle u_y(a,t)u_y(a,p)\frac{y(a,t)y(a,p)}{r(a,t)r(a,p)}\right\rangle \mathrm{d}p + \int_0^t \left\langle u_z(a,t)u_z(a,p)\frac{z(a,t)z(a,p)}{r(a,t)r(a,p)}\right\rangle \mathrm{d}p, \tag{B 5}$$

where u_x, u_y, u_z and x, y, z denote the Cartesian components of vectors $\boldsymbol{u}$ and $\boldsymbol{x}$, respectively.

In homogeneous turbulence the velocity vector $\boldsymbol{u}$ is uncorrelated with the position vector $\boldsymbol{x}$. Also, due to isotropy, the Lagrangian autocorrelation functions of all components of velocity is the same. In light of these simplifications, the above equation becomes

$$\frac{1}{2}\frac{\mathrm{d}\sigma^2}{\mathrm{d}t} = \int_0^t \langle u_x(a,t)u_x(a,p)\rangle \left\langle \frac{\boldsymbol{x}(a,t)\cdot\boldsymbol{x}(a,p)}{|\boldsymbol{x}(a,t)|\,|\boldsymbol{x}(a,p)|}\right\rangle \mathrm{d}p, \tag{B 6}$$

with a dependence on the mean cosine of the angle between radial vectors on Lagrangian trajectories. Simplifying the above as in Taylor (1922), we obtain

$$\frac{1}{2}\frac{\mathrm{d}\sigma^2}{\mathrm{d}t} = u'(t)\int_0^t u'(p) f_L(p,t)\langle\cos\alpha_{p,t}\rangle\,\mathrm{d}p, \tag{B 7}$$

where f_L denotes the Lagrangian autocorrelation function in decaying isotropic turbulence

$$f_L(t_1,t_2) \equiv \frac{\langle u_x(a,t_1)u_x(a,t_2)\rangle}{u'(t_1)u'(t_2)}, \tag{B 8}$$

where $u'(t)$ is the turbulence intensity at time t.

In (B 7), $\alpha_{p,t}$ is the angle between position vectors on the Lagrangian trajectory at times t and p. This implies that Taylor's theory overestimates the variance, since $\cos\alpha_{p,t} \leqslant 1$. The orientation factor $\langle\cos\alpha_{p,t}\rangle$ depends on the lateral movement of particles in the polar and azimuthal directions compared to that in the radial one and is close to unity for small values of the ratio between the two.

REFERENCES

Abdel-Gayed, R. G. & Bradley, D. 1977 Dependence of turbulent burning velocity on turbulent Reynolds number and ratio of flaminar burning velocity to r.m.s. turbulent velocity. *Symp. (Int.) Combust.* **16** (1), 1725–1735.

Abdel-Gayed, R. G., Bradley, D. & Gray, P. 1981 A two-eddy theory of premixed turbulent flame propagation. *Phil. Trans. R. Soc. Lond.* A **301** (1457), 1–25.

Ahmed, I. & Swaminathan, N. 2013 Simulation of spherically expanding turbulent premixed flames. *Combust. Sci. Technol.* **185** (10), 1509–1540.

Ahmed, I. & Swaminathan, N. 2014 Simulation of turbulent explosion of hydrogen–air mixtures. *Intl J. Hydrogen Energ.* **39** (17), 9562–9572.

Albin, E. 2010 Contribution to numerical modelling of turbulent flames: DNS-EEM comparisons. PhD thesis, Rouen, INSA.

Albin, E. & D'Angelo, Y. 2012 Assessment of the evolution equation modelling approach for three-dimensional expanding wrinkled premixed flames. *Combust. Flame* **159** (5), 1932–1948.

ANDREWS, G. E., BRADLEY, D. & LWAKABAMBA, S. B. 1975 Measurement of turbulent burning velocity for large turbulent Reynolds numbers. *Symp. (Int.) Combust.* **15** (1), 655–664.

BAINES, W. D. & PETERSON, E. G. 1951 An investigation of flow through screens. *Trans. Am. Soc. Mech. Engrs* **73**, 467–480.

BATCHELOR, G. K. & TOWNSEND, A. A. 1948*a* Decay of isotropic turbulence in the initial period. *Proc. R. Soc. Lond.* A **193** (1035), 539–558.

BATCHELOR, G. K. & TOWNSEND, A. A. 1948*b* Decay of turbulence in the final period. *Proc. R. Soc. Lond.* A **194** (1039), 527–543.

BATCHELOR, G. K. & TOWNSEND, A. A. 1956 Turbulent diffusion. In *Surveys in Mechanics* (ed. G. K. Batchelor & R. M. Davies). Cambridge University Press.

BIRD, R. B., STEWART, W. E. & LIGHTFOOT, E. N. 2006 *Transport Phenomena*, 2nd edn. John Wiley & Sons.

BORGHI, R. 1985 *On the Structure and Morphology of Turbulent Premixed Flames*, pp. 117–138. Springer.

BRAY, K. N. C. & LIBBY, P. A. 1986 Passage times and flamelet crossing frequencies in premixed turbulent combustion. *Combust. Sci. Technol.* **47** (5–6), 253–274.

BRAY, K. N. C., LIBBY, P. A. & MOSS, J. B. 1984 Flamelet crossing frequencies and mean reaction rates in premixed turbulent combustion. *Combust. Sci. Technol.* **41** (3–4), 143–172.

BRAY, K. N. C. & MOSS, J. B. 1977 A unified statistical model of the premixed turbulent flame. *Acta Astronaut.* **4** (3–4), 291–319.

CANT, R. S. & BRAY, K. N. C. 1989 Strained laminar flamelet calculations of premixed turbulent combustion in a closed vessel. *Symp. (Int.) Combust.* **22** (1), 791–799.

CHAKRABORTY, N. & CANT, R. S. 2005 Effects of strain rate and curvature on surface density function transport in turbulent premixed flames in the thin reaction zones regime. *Phys. Fluids* **17** (6), 065108.

CHAUDHURI, S., AKKERMAN, V. & LAW, C. K. 2011 Spectral formulation of turbulent flame speed with consideration of hydrodynamic instability. *Phys. Rev.* E **84** (2), 026322.

CHAUDHURI, S., WU, F. & LAW, C. K. 2013 Scaling of turbulent flame speed for expanding flames with Markstein diffusion considerations. *Phys. Rev.* E **88**, 033005.

CHAUDHURI, S., WU, F., ZHU, D. & LAW, C. K. 2012 Flame speed and self-similar propagation of expanding turbulent premixed flames. *Phys. Rev. Lett.* **108** (4), 044503.

CHORIN, A. J. 1968 Numerical solution of the Navier–Stokes equations. *Math. Comput.* **22**, 745–762.

CIFUENTES, L., DOPAZO, C., MARTIN, J. & JIMENEZ, C. 2014 Local flow topologies and scalar structures in a turbulent premixed flame. *Phys. Fluids* **26** (6), 065108.

COMTE-BELLOT, G. & CORRSIN, S. 1971 Simple Eulerian time correlation of full-and narrow-band velocity signals in grid-generated, isotropic turbulence. *J. Fluid Mech.* **48** (2), 273–337.

CRETA, F., LAMIONI, R., LAPENNA, P. E. & TROIANI, G. 2016 Interplay of Darrieus–Landau instability and weak turbulence in premixed flame propagation. *Phys. Rev.* E **94**, 053102.

DAMKÖHLER, G. 1940 Der einflußder turbulenz auf die flammengeschwidigkeit in gasgemischen. *Z. Elektrochem.* **46**, 601–652 (translation in NASA *Tech. Memo.* 1112 (1947)).

DARRIEUS, G. 1938 Propagation d'un front de flamme. *La Technique Moderne* **30**, 18.

DESCHAMPS, B., BOUKHALFA, A., CHAUVEAU, C., GÖKALP, I., SHEPHERD, I. G. & CHENG, R. K. 1992 An experimental estimation of flame surface density and mean reaction rate in turbulent premixed flames. *Symp. (Int.) Combust.* **24** (1), 469–475.

DESJARDINS, O., BLANQUART, G., BALARAC, G. & PITSCH, H. 2008 High order conservative finite difference scheme for variable density low Mach number turbulent flows. *J. Comput. Phys.* **227** (15), 7125–7159.

FALGOUT, R. D., JONES, J. E. & YANG, U. M. 2006 The design and implementation of Hypre, a library of parallel high performance preconditioners. In *Numerical Solution of Partial Differential Equations on Parallel Computers*, pp. 267–294. Springer.

FOGLA, N., CRETA, F. & MATALON, M. 2013 Influence of the Darrieus–Landau instability on the propagation of planar turbulent flames. *Proc. Combust. Inst.* **34** (1), 1509–1517.

FRIES, D., OCHS, B., SAHA, A., RANJAN, D. & MENON, S. 2019 Flame speed characteristics of turbulent expanding flames in a rectangular channel. *Combust. Flame* **199**, 1–13.

HINDMARSH, A. C., BROWN, P. N., GRANT, K. E., LEE, S. L., SERBAN, R., SHUMAKER, D. E. & WOODWARD, C. S. 2005 SUNDIALS: suite of nonlinear and differential/algebraic equation solvers. *ACM Trans. Math. Softw.* **31**, 363–396.

HINZE, J. O. 1975 *Turbulence*. McGraw-Hill.

HIRSCHFELDER, J., CURTISS, C., BIRD, R. & MAYER, M. 1954 *Molecular Theory of Gases and Liquids*. Wiley.

HUANG, M. J. & LEONARD, A. 1995 Velocity autocorrelations of decaying isotropic homogeneous turbulence. *Phys. Fluids* **7** (10), 2455–2464.

HUH, K. Y., KWON, J. & LEE, D. 2013 Relationships for maximum flame surface density and brush thickness through conditional analysis in turbulent premixed combustion. *Phys. Fluids* **25** (7), 075108.

JIANG, L. J., SHY, S. S., LI, W. Y., HUANG, H. M. & NGUYEN, M. T. 2016 High-temperature, high-pressure burning velocities of expanding turbulent premixed flames and their comparison with bunsen-type flames. *Combust. Flame* **172**, 173–182.

JOHNSON, N. L., KOTZ, S. & BALAKRISHNAN, N. 1994 *Continuous Univariate Distributions*, 2nd edn. Wiley-Interscience.

KIM, J. & MOIN, P. 1985 Application of a fractional-step method to incompressible Navier–Stokes equations. *J. Comput. Phys.* **59** (2), 308–323.

KOBAYASHI, H., SEYAMA, K., HAGIWARA, H. & OGAMI, Y. 2005 Burning velocity correlation of methane/air turbulent premixed flames at high pressure and high temperature. *Proc. Combust. Inst.* **30** (1), 827–834.

KOBAYASHI, H., TAMURA, T., MARUTA, K., NIIOKA, T. & WILLIAMS, F. A. 1996 Burning velocity of turbulent premixed flames in a high-pressure environment. *Symp. (Int.) Combust.* **26** (1), 389–396.

KOLLA, H., ROGERSON, J. W. & SWAMINATHAN, N. 2010 Validation of a turbulent flame speed model across combustion regimes. *Combust. Sci. Technol.* **182** (3), 284–308.

LANDAU, L. D. 1944 On the theory of slow combustion. *Acta Physicochim. USSR* **19**, 77–85.

LIBBY, P. A. & BRAY, K. N. C. 1980 Implications of the laminar flamelet model in premixed turbulent combustion. *Combust. Flame* **39** (1), 33–41.

LIBBY, P. A. & WILLIAMS, F. A. 1994 *Turbulent Reacting Flows*. Academic Press.

LIPATNIKOV, A. 2012 *Fundamentals of Premixed Turbulent Combustion*. CRC Press.

LIPATNIKOV, A. N. & CHOMIAK, J. 2002 Turbulent flame speed and thickness: phenomenology, evaluation, and application in multi-dimensional simulations. *Prog. Energy Combust. Sci.* **28** (1), 1–74.

LIU, C. C., SHY, S. S., PENG, M. W., CHIU, C. W. & DONG, Y. C. 2012 High-pressure burning velocities measurements for centrally-ignited premixed methane/air flames interacting with intense near-isotropic turbulence at constant Reynolds numbers. *Combust. Flame* **159**, 2608–2619.

LIU, X. D., OSHER, S. & CHAN, T. 1994 Weighted essentially non-oscillatory schemes. *J. Comput. Phys.* **115**, 200–212.

LUCA, S., AL-KHATEEB, A. N., ATTILI, A. & BISETTI, F. 2018*a* Comprehensive validation of skeletal mechanism for turbulent premixed methane–air flame simulations. *J. Propul. Power* **34**, 153–160.

LUCA, S., ATTILI, A., LO SCHIAVO, E., CRETA, F. & BISETTI, F. 2018*b* On the statistics of flame stretch in turbulent premixed jet flames in the thin reaction zone regime at varying Reynolds number. *Proc. Combust. Inst.* **37** (2), 2451–2459.

MATHUR, S., TONDON, P. K. & SAXENA, S. C. 1967 Thermal conductivity of binary, ternary and quaternary mixtures of rare gases. *Mol. Phys.* **12**, 569–579.

MAZ'YA, V. 1985 *Sobolev Spaces*, chap. 1.2.4, p. 37. Springer.

MCBRIDE, B. J., GORDON, S. & RENO, M. A. 1993 Coefficients for calculating thermodynamic and transport properties of individual species. NASA *Tech. Memo. 4513*.

MOHAMED, M. S. & LARUE, J. C. 1990 The decay power law in grid-generated turbulence. *J. Fluid Mech.* **219**, 195–214.

MUELLER, B. 1999 Low Mach number asymptotics of the Navier–Stokes equations and numerical implications. In *Lecture Series, von Kármán Institute for Fluid Dynamics*.

PEACEMAN, D. W. & RACHFORD, H. H. 1955 The numerical solution of parabolic and elliptic differential equations. *J. Soc. Ind. Appl. Maths* **3**, 28–41.

PETERS, N. 1988 Laminar flamelet concepts in turbulent combustion. *Symp. (Int.) Combust.* **21** (1), 1231–1250.

PETERS, N. 1992 A spectral closure for premixed turbulent combustion in the flamelet regime. *J. Fluid Mech.* **242**, 611–629.

PETERS, N. 1999 The turbulent burning velocity for large-scale and small-scale turbulence. *J. Fluid Mech.* **384**, 107–132.

PETERS, N. 2000 *Turbulent Combustion*. Cambridge University Press.

PIERCE, C. D. 2001 Progress-variable approach for large-eddy simulation of turbulent combustion. PhD thesis, Stanford University.

POCHEAU, A. 1992 Front propagation in a turbulent medium. *Europhys. Lett.* **20** (5), 401–406.

POINSOT, T. & VEYNANTE, D. 2012 *Theoretical and Numerical Combustion*, 3rd edn. Centre Européen de Recherche et de Formation Avancée en Calcul Scientifique.

POPE, S. B. 1988 The evolution of surfaces in turbulence. *Intl J. Engng Sci.* **26** (5), 445–469.

POPE, S. B. 2000 *Turbulent Flows*. Cambridge University Press.

RENOU, B., MURA, A., SAMSON, E. & BOUKHALFA, A. 2002 Characterization of the local flame structure and the flame surface density for freely propagating premixed flames at various Lewis numbers. *Combust. Sci. Technol.* **174** (4), 143–179.

ROSALES, C. & MENEVEAU, C. 2005 Linear forcing in numerical simulations of isotropic turbulence: physical space implementations and convergence properties. *Phys. Fluids* **17** (9), 095106.

SHY, S. S., LEE, E. I., CHANG, N. W. & YANG, S. I. 2000 Direct and indirect measurements of flame surface density, orientation, and curvature for premixed turbulent combustion modeling in a cruciform burner. *Proc. Combust. Inst.* **28** (1), 383–390.

SINHUBER, M., BODENSCHATZ, E. & BEWLEY, G. P. 2015 Decay of turbulence at high Reynolds numbers. *Phys. Rev. Lett.* **114**, 034501.

SMITH, G. P., GOLDEN, D. M., FRENKLACH, M., MORIARTY, N. W., EITENEER, B., GOLDENBERG, M., BOWMAN, C. T., HANSON, R. K, SONG, S., GARDINER JR., W. C., *et al.* 1999 Gri-mech version 3.0. Available at: http://combustion.berkeley.edu/gri-mech/version30/text30.html.

TAYLOR, G. I. 1922 Diffusion by continuous movements. *Proc. R. Soc. Lond.* A **2** (1), 196–212.

TAYLOR, G. I. 1935 Statistical theory of turbulence. *Proc. R. Soc. Lond.* A **151** (873), 421–444.

TOMBOULIDES, A. G., LEE, J. C. Y. & ORSZAG, S. A. 1997 Numerical simulation of low Mach number reactive flows. *J. Sci. Comput.* **12** (2), 139–167.

TROUVÉ, A. & POINSOT, T. 1994 The evolution equation for the flame surface density in turbulent premixed combustion. *J. Fluid Mech.* **278**, 1–31.

VERVISCH, L., BIDAUX, E., BRAY, K. & KOLLMANN, W. 1995 Surface density function in premixed turbulent combustion modeling, similarities between probability density function and flame surface approaches. *Phys. Fluids* **7** (10), 2496–2503.

VEYNANTE, D., DUCLOS, J. M. & PIANA, J. 1994 Experimental analysis of flamelet models for premixed turbulent combustion. *Symp. (Int.) Combust.* **25** (1), 1249–1256.

WILKE, C. R. 1950 A viscosity equation for gas mixtures. *J. Chem. Phys.* **18**, 517–519.

WU, F., SAHA, A., CHAUDHURI, S. & LAW, C. K. 2015 Propagation speeds of expanding turbulent flames of C_4 to C_8 *n*-alkanes at elevated pressures: experimental determination, fuel similarity, and stretch-affected local extinction. *Proc. Combust. Inst.* **35** (2), 1501–1508.

YANG, S., SAHA, A., LIU, Z. & LAW, C. K. 2018 Role of Darrieus–Landau instability in propagation of expanding turbulent flames. *J. Fluid Mech.* **850**, 784–802.

ZHENG, T., YOU, J. & YANG, Y. 2017 Principal curvatures and area ratio of propagating surfaces in isotropic turbulence. *Phys. Rev. Fluids* **2** (10), 103201.